

Experiments and Modeling in Support of Generic Salt Repository Science

Fuel Cycle Research & Development

*Prepared for
U.S. Department of Energy
Used Fuel Disposition Campaign
Milestone M3FT-16LA080309011*

*S.M. Bourret,
P.J. Johnson
G.A. Zyvoloski
S.P. Chu
D.J. Weaver
S. Otto
H. Boukhalfa
F.A. Caporuscio
A.B. Jordan
P.H. Stauffer*

*Los Alamos National Laboratory
September 30, 2016*

Los Alamos National Laboratory Document
LA-UR-16-27329
FCRD-UFD-2016-000445



DISCLAIMER

This information was prepared as an account of work sponsored by an agency of the U.S. Government. Neither the U.S. Government nor any agency thereof, nor any of their employees, makes any warranty, expressed or implied, or assumes any legal liability or responsibility for the accuracy, completeness, or usefulness, of any information, apparatus, product, or process disclosed, or represents that its use would not infringe privately owned rights. References herein to any specific commercial product, process, or service by trade name, trade mark, manufacturer, or otherwise, does not necessarily constitute or imply its endorsement, recommendation, or favoring by the U.S. Government or any agency thereof. The views and opinions of authors expressed herein do not necessarily state or reflect those of the U.S. Government or any agency thereof.

FCT Quality Assurance Program Document

Appendix E FCT Document Cover Sheet

Test Proposal Document for Phased Field Thermal Testing in Salt

Name/Title of Deliverable/Milestone

Work Package Title and Number

Work Package WBS Number

Responsible Work Package Manager

FT-16LA08030901

DR Salt R&D - LANL

1.02.08.03.09

Philip H. Stauffer

(Name/Signature)

Date Submitted

Quality Rigor Level for
Deliverable/Milestone☒ QRL-3☐ QRL-2☐ QRL-1☐ Nuclear Data☐ N/A*

This deliverable was prepared in accordance with

Los Alamos National Laboratory

(Participant/National Laboratory Name)

QA program which meets the requirements of

☒ DOE Order 414.1☐ NQA-1-2000**This Deliverable was subjected to:**☐ Technical Review**Technical Review (TR)****Review Documentation Provided**☐ Signed TR Report or,☐ Signed TR Concurrence Sheet or,☒ Signature of TR Reviewer(s) below**Name and Signature of Reviewers**

Hari Viswanathan

☐ Peer Review**Peer Review (PR)****Review Documentation Provided**☐ Signed PR Report or,☐ Signed PR Concurrence Sheet or,☐ Signature of PR Reviewer(s) below

*Note: In some cases there may be a milestone where an item is being fabricated, maintenance is being performed on a facility, or a document is being issued through a formal document control process where it specifically calls out a formal review of the document. In these cases, documentation (e.g., inspection report, maintenance request, work planning package documentation or the documented review of the issued document through the document control process) of the completion of the activity along with the Document Cover Sheet is sufficient to demonstrate achieving the milestone. QRL for such milestones may be also be marked N/A in the work package provided the work package clearly specifies the requirement to use the Document Cover Sheet and provide supporting documentation.

Table of Contents

List of Figures	V
List of Tables	VII
1 Introduction	1
2 FEHM Updates	2
2.1 Code corrections and additions	2
3 Test Problems	4
3.1 p_{ngas} for water vapor	4
3.1.1 Test 1: Constant temperature with a specified air relative humidity for in-flow	4
3.1.2 Test 2a: increasing temperature across the domain	7
3.1.3 Test 2b: decreasing temperature across the domain	8
3.2 Water vapor pressure	10
3.2.1 Grid parameters and model setup	11
3.2.2 Results	11
4 Salt Tube Modeling	14
4.1 Experiment description	14
4.1 First model test (no insulating layers)	15
4.2 Second model test (with insulating layers)	18
5 Pan evaporation experiment modeling	22
5.1 Experiment description	22
5.2 Model setup	23
5.3 fxa test runs	24
5.4 Test of fxa with air flow	24
6 Brine Transport Experiments in RoM Salt	25
6.1 Introduction	25
6.1.1 Objectives	26
6.1.2 Background	27
6.2 Experimental method	28
6.2.1 Salt box setup	28
6.2.2 Temperature profile mapping	31
6.2.3 Tracer injections	32

Experiments and Modeling in Support of Generic Salt Repository Science

6.2.4	Post heating forensics - Salt dissolution and re-precipitation in sea salt experiment	33
6.3	Results and Discussion.....	33
6.3.1	Temperature profile in RoM salt experimental data and modeling	33
6.3.2	Water vapor behavior in RoM salt.....	37
6.3.3	Tracer breakthrough experimental data and modeling	39
6.3.4	Post heating forensics examination of salt dissolution and re-precipitation.....	45
7	Reanalysis of salt canister.....	49
7.1	Objectives.....	49
7.2	Model setup.....	49
7.3	Results	50
8	Future Work.....	52
	References.....	53
	Appendix A: Additions and Usage of New Humidity Boundary Conditions.....	56

List of Figures

Figure 1: Model domain conceptualization, where RH is the relative humidity (-), n is the porosity (-), $\theta_s - initial$ is the initial saturation (-), K is the rock permeability (m^2), and ΔP is the pressure change between the right and left boundaries (Pa).....	4
Figure 2: Maximum relative humidity curve shows the water vapor holding capacity of air at increasing temperatures.	5
Figure 3: Comparison of FEMH and PFLOTRAN to the analytical solution for test problem 1.	6
Figure 4: Model domain conceptualization for Test 2a, where RH is the relative humidity (-), n is the porosity (-), $\theta_s - initial$ is the initial saturation (-), K is the rock permeability (m^2), and ΔP is the pressure change between the right and left boundaries (Pa).....	7
Figure 5: Comparison of FEHM results to the analytical solution.	8
Figure 6: Model domain conceptualization for Test 2b, where RH is the relative humidity (-), n is the porosity (-), $\theta_s - initial$ is the initial saturation (-), K is the rock permeability (m^2), and ΔP is the pressure change between the right and left boundaries (Pa).....	9
Figure 7: Comparison of FEHM results to the analytical solution for Test 2b.....	10
Figure 8: Model setup for Pwv test problem; numbers indicate temperature.	11
Figure 9: Desalinated water Pwv values (black), predicted 75% values (red line), 2015 model results (green), and early 2016 model results (blue), showing inaccurate Pwv values following amendments to vaporl_salt.f.....	12
Figure 10: June 6 corrected values (purple) added to previous plot, showing corrected values after patch applied to vaporl_salt.f.....	13
Figure 11: Experimental setup from Olivella et al. (2011).	14
Figure 12: Model domain for case with no insulating layers.....	15
Figure 13: Observed salt tube porosity changes over time, from Olivella et al. (2011). Note the considerable increase at the low-temperature (right) side as time increases.....	16
Figure 14: FEHM modeled porosity changes over time for a perfectly insulated salt tube. Porosity increases are primarily near the center of the tube.	17
Figure 15: Temperature profile (a) and maximum relative humidity curve compared to temperature (b). Maximum relative humidity changes most rapidly above $T=50^\circ\text{C}$, so porosity changes would be expected to be most dominant in the warmer portion of the salt tube.....	17
Figure 16: Model domain with insulated layers.....	18
Figure 17: Temperature contours with added insulating layers.	19
Figure 18: Porosity contours with added insulating layers.	20
Figure 19: Temperature profiles for (a) simulations with no insulating layers (b) simulation including insulating layers. Discrepancies can be attributed to thermal conduction through insulating layers and minor differences in heat flow when porosity changes. Temperature profiles are notably depressed on the warm end in the insulated case.	21
Figure 20: Differences in porosity in (a) no-insulator and (b) insulated cases. Center-domain porosities are comparable, but the case including insulators shows a slight increase at the cold end.	21
Figure 21: Conceptual model of water vapor pressure for desalinated water (blue), water containing NaCl salt (green), and water containing WIPP salt with impurities (yellow); salt and impurities depress water vapor pressure.....	22
Figure 22: Salt pan experiment in WIPP salt gallery. Pans with salt piles are on left.	23

Experiments and Modeling in Support of Generic Salt Repository Science

Figure 23: Model domain for salt pan experiment.....	24
Figure 24: Mass change (%) of salt cone, showing comparison of FEHM model results (blue) to lab measurements (red).	25
<i>Figure 25: Heat pipe in salt.</i>	27
Figure 26: Pictures A and B show a salt enclosure (salt box) filled with RoM salt used in our experiments. (1) Temperature controller, (2) heating block power supply, (3) RH logger, (4) thermocouple bundle, (5) Plexiglas enclosure.	28
Figure 27: Schematic representation of a salt box filled with RoM salt and instrumented with a heater thermocouples a relative humidity probe and gas sampling and injection ports.....	30
Figure 28: Infrared imaging of salt box at maximum temperature of 260 °C.....	32
Figure 29: Temperature profile with time for the thermocouples placed at different distances from the heat source. The heating block was set at 50 °C and the closest thermocouple (highest temperatures) was set at 6.35 cm from the heater.	34
Figure 30: Temperature profiles at a set point 2.5 inches from the heat source. The heat source temperature was fixed at the indicated temperatures using a temperature controller and was turned off after temperature of the salt reached a steady state and let cool down to ambient temperature.....	34
Figure 31: Temperature distribution in a RoM salt as a function of the distance from the heat source. The different lines represent independent runs performed by fixing the temperature of the heat source to the indicated temperatures.	35
Figure 32: Thermal conductivity of RoM salt based on the BAMBUSII experiments. (a) shows thermal conductivity dependence on porosity (Equation 3) and (b) shows a thermal conductivity curve changing with temperature for salt with porosity = 0.3 (Equation 4).	36
Figure 33: Simulated steady-state temperatures for all thermocouples compared to measured temperatures for three simulation (80, 160, and 260 °C), plotted against the 1:1 line. Note the warm colors are locations close to the heater, the farther locations are represented by cooler colors.	37
Figure 34: Relative humidity in the airspace above the salt in a box filled with granular salt with 2.0 wt.% brine ponded at the bottom of the salt box.	37
Figure 35: Relative humidity in the air space above the RoM salt under ambient conditions and when the heating block is powered to 80 °C.....	38
<i>Figure 36: Relative humidity in the air gap above the salt and in the air flow circulated through salt. The experiment was performed at ambient temperature of 23.5 °C. The salt properties are summarized in Table 5.</i>	39
<i>Figure 37: Breakthrough curves for tracer gases SF6 (experimental data = squares, fit = solid line) and Chloroform (experimental data = diamonds, fit = dotted line) performed under ambient temperature conditions before heating. Tracer test T1.</i>	40
Figure 38: Schematic representation of the tracer test performed under ambient temperature conditions immediately after setting up the salt box. Conditions: Temperature = 23.5 °C, Air flow recirculation, Heater temperature = ambient, salt height = 19 inches, moisture content in salt 0.19 wt.%, RH in air gap = 15%.	40
<i>Figure 39: Breakthrough curves of tracer gases at ambient temperature and at 80 °C. Filled and empty diamonds show the breakthrough of SF6 at ambient conditions and following heating at 80 °C for 24 hours and after two weeks. Filled squares and stars filled squares show the breakthrough of Chloroform at ambient conditions and following heating at 80 °C for 24 hours. Tracer tests T2 and T3.</i>	42

Experiments and Modeling in Support of Generic Salt Repository Science

Figure 40: Schematic representation of tracer tests performed under heating conditions. The schematics show a convection process that pushes hot air to the air gap and recirculates cold air back to the bottom of the box. Temperature = 80 °C, Air flow recirculation, Heater temperature = ambient, salt height = 19 inches, moisture content in salt 0.19 wt.%, RH in air gap = 35%	43
<i>Figure 41: Tracer breakthrough results showing data for SF6 and Chloroform at different temperatures. Triangles represent Chloroform breakthrough and squares represent data for SF6. The different temperatures are indicated in the figure caption.</i>	<i>44</i>
<i>Figure 42: Sample S-30</i>	<i>46</i>
Figure 43: Sample S-31	47
Figure 44: Sample S-34	47
Figure 45: Sample S-36	48
<i>Figure 46: Sample S-38</i>	<i>48</i>
Figure 47: Salt canister model domain. Canisters are shown in orange, damaged salt in yellow, air in blue, and intact salt in green.....	50
Figure 48: Comparison of “hacked” FEHM code model run performance vs. the August 2016 model version. The rate of model time advancement (a), the CPU time necessary for the model to run (b), Newton-Raphson iterations (c), and total Solver iterations (d) are compared.....	51

List of Tables

Table 1: Changes to FEHM routines.	3
Table 2: x-distance vs. temperature specified at each node.....	11
Table 3: Salt properties used in modeling.....	15
Table 4: Insulating layer properties.	19
Table 5: Properties of the bulk RoM salt used in the experiments.	29
Table 6: Summary of the specifics of the salt box used in the experiments.....	31
Table 7: Summary of the tracer test performed in RoM salt.	41
Table 8: Porosity data of forensic samples. Depth and porosity information from excavated samples.	45
Table 9: Parameters of difference between intact and damaged salt for canister runs.	50

1 Introduction

Salt is an attractive material for the disposition of heat generating nuclear waste (HGNW) because of its self-sealing, viscoplastic, and reconsolidation properties (*Hansen and Leigh, 2012*). The rate at which salt consolidates and the properties of the consolidated salt depend on the composition of the salt, including its content in accessory minerals and moisture, and the temperature under which consolidation occurs. Physicochemical processes, such as mineral hydration/dehydration salt dissolution and precipitation play a significant role in defining the rate of salt structure changes. Understanding the behavior of these complex processes is paramount when considering safe design for disposal of heat-generating nuclear waste (HGNW) in salt formations, so experimentation and modeling is underway to characterize these processes.

This report presents experiments and simulations in support of the DOE-NE Used Fuel Disposition Campaign (UFDC) for development of drift-scale, in-situ field testing of HGNW in salt formations. Several bench-scale/lab-scale experiments have recently been performed to provide opportunities for numerical code verification and validation, in support of proposed underground tests of heat and mass transfer around a heat source. Such simulations provide crucial insight for the safe design and monitoring of future larger-scale in-situ tests and support the long term safety basis for possible HGNW repositories in salt.

Simulations described in this report employ the Finite Element Heat and Mass Transfer code (FEHM, <https://fehm.lanl.gov>). Although this code was originally intended to simulate geothermal reservoirs (Kelkar et al., 2011), subsequent revisions and additions in the past 30 years (Zyvoloski et al., 1997; Zyvoloski, 2007) have allowed simulation of complex hydrologic systems including unsaturated flow, reactive chemistry, stress, and carbon dioxide transport. FEHM uses a finite volume method for solving multiphase flow and transport, while using a finite element formulation for the fully coupled stress solutions. Recent additions to FEHM are described in Stauffer et al. (2013) and Jordan et al. (2015a,b). These additions consist of a new module specifically designed for simulation of salt, as well as minor changes to the fundamental FEHM code. Subsequent code modifications have been implemented for numerical efficiency and accuracy and are reported herein.

Much of the work presented in this report builds on previous experimental work and associated modeling described in Jordan et al. (2015b) and Stauffer et al. (2015). The overall modeling objective is to ensure that changes and new capabilities added to the FEHM code are functioning properly and reproducing the complex multiphase processes observed in salt. Current HGNW salt disposition research focuses on the Waste Isolation Pilot Plant (WIPP) near Carlsbad, NM; salt in this formation is more complex than “pure” NaCl salt (Krieg, 1984; Lappin, 1988). Prior to conducting numerical simulations at in-situ conditions, it is useful to first ensure proper model function by comparing model results to relatively simple experimental results using well-established parameters of salt determined in the laboratory.

Section 2 of this milestone describes code amendments. Next, we present verification/validation exercises that compare to simulated results with analytical solutions in Section 3. Section 4 revisits the modeling work of Olivella et al. (2011), a bench-scale

experiment that is a sensitive check for FEHM and other numerical simulators. Section 5 describes modeling work related to bench-scale experiments conducted in WIPP salt. Section 6 covers the bench-scale experiments performed at LANL. Finally Section 7 discusses numerical improvements in our simulations of hypothetical drift scale experiments.

2 FEHM Updates

2.1 Code modifications

Amendments to FEHM code this year primarily involve modifications to the previous version of the salt module. A brief description of changes to individual code segments is described in Table 1. Minor changes were made to subroutines in order to increase efficiency, reduce the number of timesteps, or reduce the time needed to complete any single timestep. To prevent instability in numerical solutions or identify improper model inputs, several non-salt modules had minor code changes. Four routines had cosmetic changes that did not alter functionality. Finally, code pertaining to temperature-dependent vapor pressure of humid air in salt was corrected to properly represent salinity-effects on the vapor pressure of air. A test problem for this is described in section 3.2.

A new set of boundary condition capabilities were added in early August 2016 to broaden the scenarios in which FEHM can be applied. In particular, the previous *fxa* macro required a gas flux through the model domain. In cases where gas flux is not appropriate for the simulation, it can be more useful to directly specify the humidity at a boundary and add or remove water as needed in order to satisfy the humidity condition. Usage and descriptions of these conditions can be found in Appendix A.

Table 1: Changes to FEHM routines.

Subroutine	Change
Allocmem.f	Added allocation on new accumulation term storage
Comai.f	Added variable to save timestep restart criteria
Comci.f	Added allocatable arrays for mass and energy storage terms
Comdi.f	Added allocatable arrays for variable humidity air inflow in boun macro (for <i>fxa</i>)
Diskread.f	Cosmetic
Dvacalc.f	Updated dva() function to improve stability of derivatives
Geneqc.f	Cosmetic
Model_setup.f	Added input for variable input of humidified air (for <i>fxa</i>)
outbnd.f	Zeroed out of bounds error code mlz
Psatl.f	Minor corrections to coding for vapor pressure lowering
Saltctr.f	Minor additions to functionality
Scanin.f	Added code to scan input files for humidity boundary condition <i>fxa</i>
User_ypm.f	Added some code for fitting solubility parameters and vapor pressure parameters
Vaporl.f	Corrections to vapor pressure lowering (see section 3.2)
Wrtout.f	Added printout for number of gridblocks in each phase state
Flow_humidity_bc.f	Added routine to calculate inlet flowrates and enthalpy for dry air and water vapor
Aircctr.f	Added coding to check for bad input temperatures for isothermal calculations
Headctr.f	Cosmetic
Thrair.f	Improved consistency and performance for seepage face models
Rlp_cap.f	Corrected error with VG relative permeability models when saturation approaches zero
Startup.f	Added call to airctr.f for checking temperatures
Flow_boundary_conditions.f	Minor changes to improve seepage face calculations
Fehmn_pcx.f	Cosmetic

3 Test Problems

3.1 *ngas* for water vapor

We constructed three simple test problems to confirm that the newly-modified macro *ngas* for FEHM (Jordan et al., 2015a) is accurately simulating flowing air with prescribed relative humidity. Comparison with analytical solutions confirm the code modifications are performing correctly. The goal is to specify relative humidity and temperature boundary conditions for flowing air to test that FEHM will transport water in vapor form in and out of a salt deposit as expected. The three test problems are: (1) dry air flows through a domain at a constant temperature and removes water from the porous salt matrix, (2a) fully-saturated air flows through the domain with temperature increasing from 25 °C to 30 °C to dry out the matrix and (2b) fully-saturated air flows through the domain with temperature decreasing from 25 °C to 19 °C to saturate the matrix. These test problems show that the FEHM *ngas* successfully dries or saturates the salt matrix depending on temperature and relative humidity conditions.

3.1.1 *Test 1: Constant temperature with a specified air relative humidity for in-flow*

The grid for all *ngas* macro tests is a 1.0 m long, 0.2 m wide 2-dimensional space (Figure 1). It is discretized into 20 square, equally-sized elements. Material properties are initially homogeneous throughout the interior of the grid. Top ($y = 0.2$ m) and bottom ($y = 0$ m) boundaries are no-slip and no-flow. Air at specified temperature and humidity flows into the model along the line of nodes at $x = 0$, and flow out at $x = 1.0$. Nodes are initially partly saturated and will become either drier or wetter as relative humidity of flowing air changes.

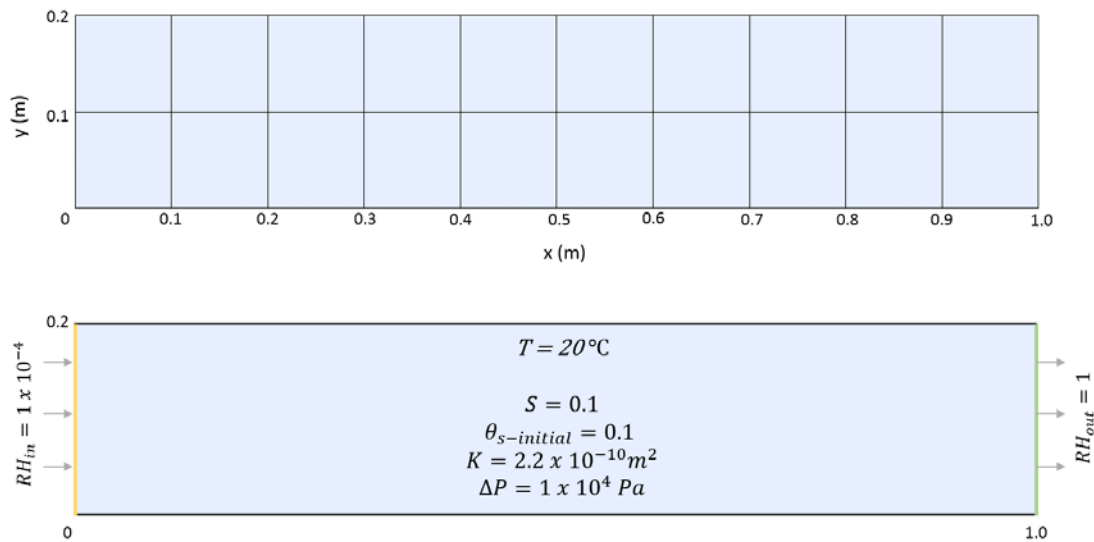


Figure 1: Model domain conceptualization, where RH is the relative humidity (-), n is the porosity (-), $\theta_{s-initial}$ is the initial saturation (-), K is the rock permeability (m^2), and ΔP is the pressure change between the right and left boundaries (Pa).

The domain has a constant temperature of 20 °C and a very low, constant pressure gradient to drive air flow of $1 \times 10^{-4} \frac{pa}{m}$. The matrix is homogenous and isothermal, assigned values 0.1 for porosity and $2.2 \times 10^{-10} m^2$ for rock permeability. The initial saturation of the matrix is 0.1, results in 2 kg of initial water mass in the system. The mass of the pore-water represents the liquid water that the dry air ($RH = 1 \times 10^{-4}$) flowing through the domain can pick up and remove from the system in the vapor phase. We assigned a relative permeability of water to a value of zero, causing the water in the matrix to only be removed by transition into the vapor phase and not flow due to the pressure gradient. The air leaving the model has a relative humidity of 1.0.

The dry air enters the box at 20° holding $1.0 \frac{g}{kg}$ of water, but has the capacity to hold $14.62 \frac{g}{kg}$ which causes the air to pick up water from the matrix as it flows through the domain. The values of air moisture-holding capacity are determined by Equation 1 and shown in Figure 2, which was based on data available from engineering toolbox (http://www.engineeringtoolbox.com/humidity-ratio-air-d_686.html):

$$\phi_s = (4.4297 \times 10^{-3}) e^{0.0594T} \quad \text{Equation 1}$$

where T is temperature (°C) and ϕ_s is the air moisture-holding capacity ($\frac{kg}{kg}$).

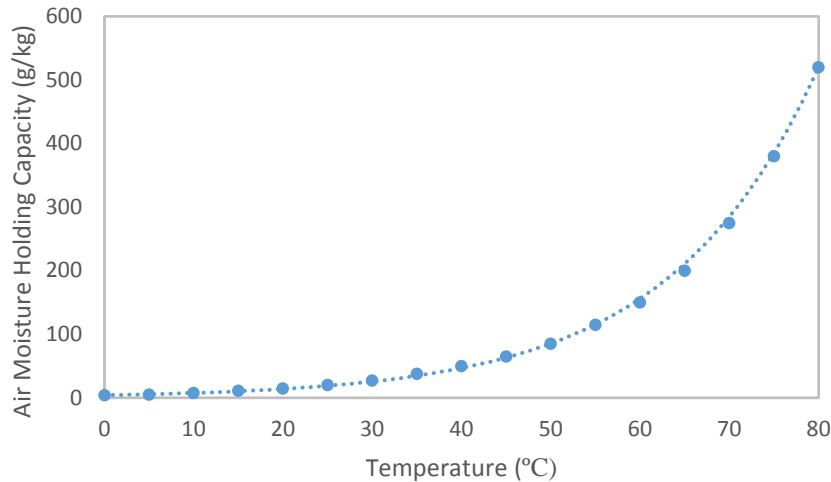


Figure 2: Maximum relative humidity curve shows the water vapor holding capacity of air at increasing temperatures.

An analytical solution was used to compare and test the correctness of the FEHM solution. The rate of water removal from the analytical solution was determined by Equation 2,

$$q_{water} = q_{air} * HR_{max} \quad \text{Equation 2}$$

where q_{water} and q_{air} is the mass flux of water and air ($\frac{kg}{s}$), and HR_{max} is the moisture holding capacity of air ($\frac{kg}{kg}$). The moisture holding capacity increases with temperature, so for this problem we expect air to pick up water as the temperature increases through the domain. The maximum air-moisture holding capacity is determined from the curve described by Equation 1.

Initial water mass, air-flow rate, temperature, and mass fraction water vapor of inflowing air were assigned the same values for the analytical solution and FEHM model. The comparison of the water-mass removal results, shown in Figure 3, are in agreement. As expected, the dry air evaporates the pore-water as it travels through the domain, thus drying out the matrix over time. The rate of water removal in the FEHM simulation matches with our simple analytical model, signifying FEHM is performing well. We also worked with Glen Hammond of Sandia National Laboratory to run the same numerical problem with PFLOTTRAN, showing results that are nearly identical to FEHM and the analytical solution.

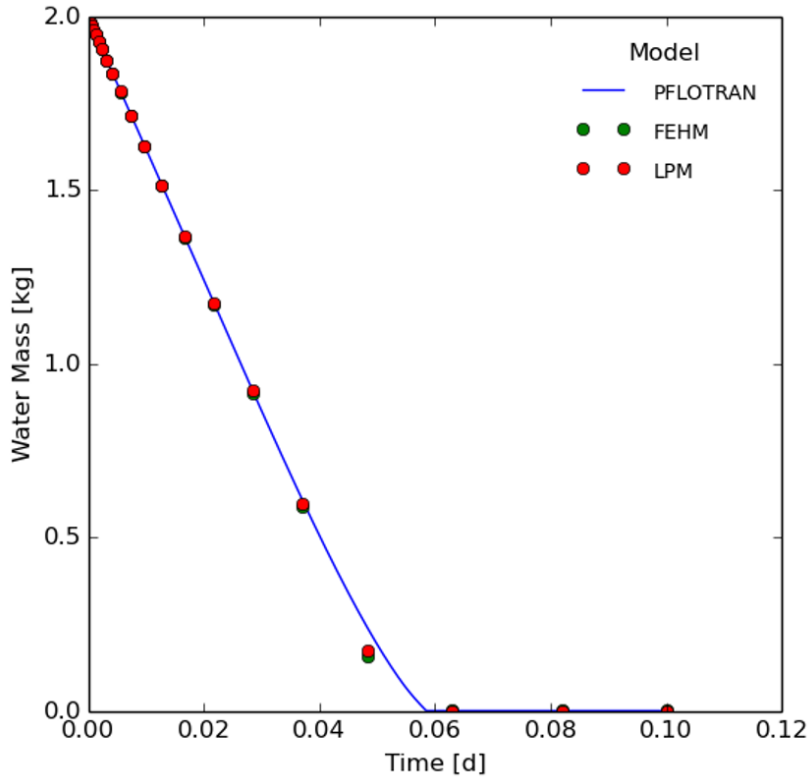


Figure 3: Comparison of FEMH and PFLOTTRAN to the analytical solution for test problem 1.

3.1.2 Test 2a: increasing temperature across the domain

The domain for Test 2a has a constant temperature gradient increasing from 25 °C on the left-hand side ($x = 0$) to 30 °C on the right-hand side ($x = 1.0$), and a very low pressure gradient ($100 \frac{Pa}{m}$) to drive air flow, resulting in a nearly constant $1.35 \times 10^{-4} \frac{kg}{s}$ air-flow rate flowing from left to right (Figure 4). Initial temperature within the model domain is defined at a single value but a gradient is rapidly established due to conduction and advection of heat through the domain. Air passing through this gradient is correspondingly heated or cooled so that the relative humidity will increase or decrease. The matrix has homogenous values of 0.1 for porosity and $1 \times 10^{-10} m^2$ for rock permeability. Initial saturation of the matrix is 0.1 resulting in 2 kg of initial water mass in the system. Since air is warming as it passes through the box it should evaporate water from pores, moistening the air and drying the porous medium.

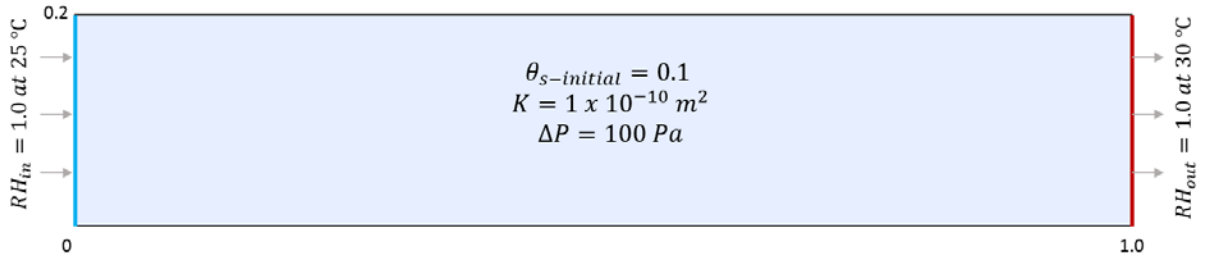


Figure 4: Model domain conceptualization for Test 2a, where RH is the relative humidity (-), n is the porosity (-), $\theta_{s-initial}$ is the initial saturation (-), K is the rock permeability (m^2), and ΔP is the pressure change between the right and left boundaries (Pa).

The air enters the box at 25°C and 100% relative humidity, holding $19.95 \frac{g}{kg}$ of water vapor. It exits at 30°C, which can hold $26.99 \frac{g}{kg}$, allowing for the air to pick up water from the matrix as it flows through the domain. The values of air moisture-holding capacity are determined by Equation 1. We assigned a relative permeability of water to a value of zero at all nodes to prevent water flow, causing the water in the matrix to only be removed by transition into the vapor phase.

Initial water mass, air-flow rate, boundary temperatures, and relative humidity of inflowing air ($RH = 100\%$) were assigned the same values in the analytical solution as in the FEHM model. The comparison of the water-mass removal results are shown in Figure 5. Results of the analytical model are in agreement with FEHM. As expected, the increased temperature allows for water to be picked up by the warming air as it travels through the domain, thus drying out the as time increases until no water remains in the matrix.

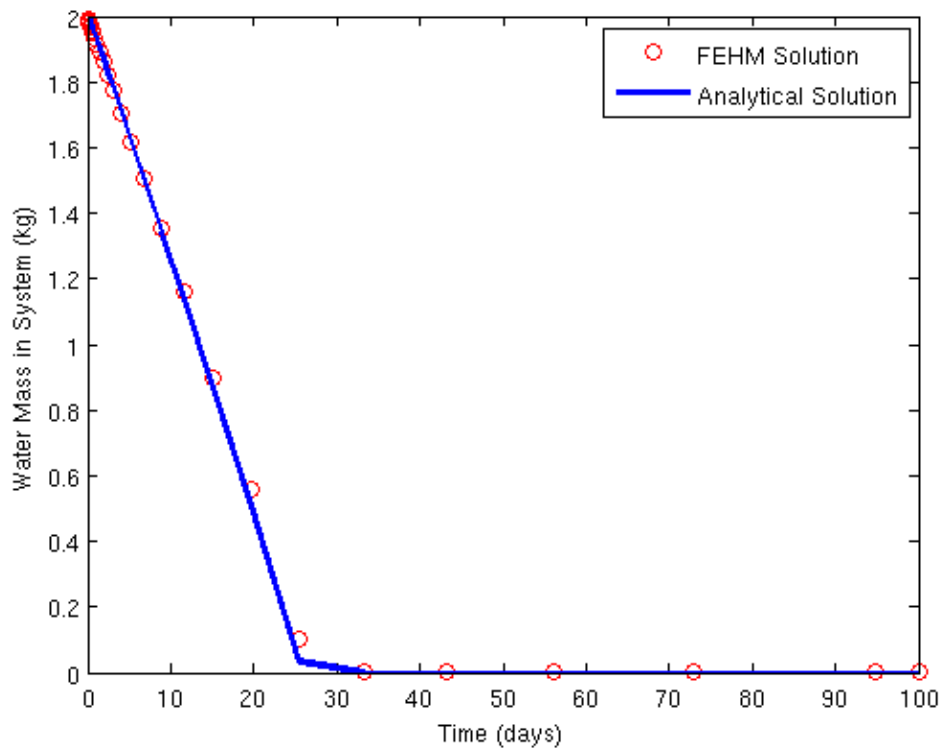


Figure 5: Comparison of FEHM results to the analytical solution.

3.1.3 Test 2b: decreasing temperature across the domain

The final *ngas* test takes the inverted approach from Test 2a. The domain has a constant temperature gradient decreasing from 25 °C to 19 °C and a low pressure gradient of $10 \frac{pa}{m}$ to drive air flow (Figure 6). In this case, saturated cooling air should condense moisture into the box; consequently the air flow rate decreases through the course of the model run due to the decrease in air volume available for flow as the domain fills with water. The matrix has homogenous values of 0.1 for porosity and $1 \times 10^{-9} m^2$ for rock permeability. The initial saturation of the matrix was set to 0.1, resulting in 2 kg of initial water mass in the system.

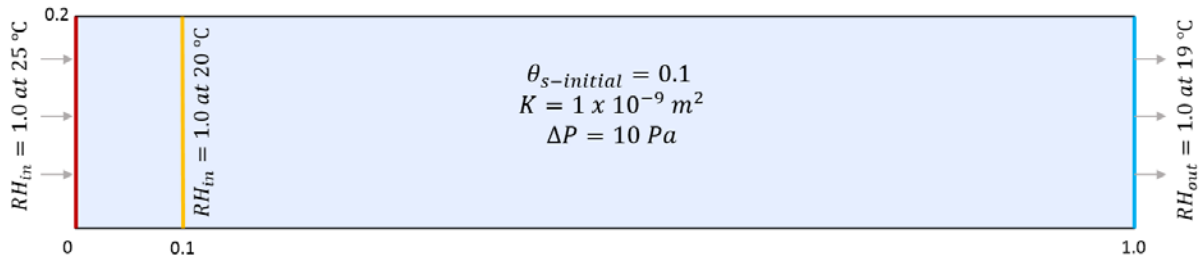


Figure 6: Model domain conceptualization for Test 2b, where RH is the relative humidity (-), n is the porosity (-), $\theta_{s-initial}$ is the initial saturation (-), K is the rock permeability (m^2), and ΔP is the pressure change between the right and left boundaries (Pa).

The air that enters and exits the box is fully saturated ($RH = 100\%$), holding $19.95 \frac{g}{kg}$ at $25\text{ }^\circ\text{C}$ and $13.72 \frac{g}{kg}$ at $19\text{ }^\circ\text{C}$, thus the wet air deposits water into the matrix as it flows through the domain. The values of air moisture-holding capacity are again determined by Equation 1.

We assigned a relative permeability of water to a value of zero at the right and left side boundaries to prevent water from flowing out of the domain, causing the water in the matrix to only be removed by transition into the vapor phase and not flow due to the pressure gradient. The relative permeability model set at the boundary nodes prevent faster saturation of the nodes at the entrance side of the domain, which would cause air flow to stop (when saturation approached 1.0) because there was no air-filled pore volume available for air flow before the remainder of the box could reach saturation. Water flow was simulated in the rest of the domain. With these relative permeability models assigned, we were able to maintain constant saturation of 0.1 at the inlet nodes, and all other nodes in the domain increased saturation over the simulation equally with an equal flowrate across the domain at each time step.

The comparison of the water-mass removal results are shown in Figure 7. The analytical solution uses the time-dependent gas-flow rates output by the FEHM simulation, and the results of the two models agree well. As expected, the decreasing temperature across the domain causes condensation of liquid water out of the cooling air due to the decreased water vapor capacity to maintain the relative humidity 100%. This results in matrix saturation approaching 1.0 as time increases; gas-flow rates approach zero as air-filled porosity reaches zero allowing for no air flow. The rate of water removal in the FEHM simulation match with our simple analytical model, showing that FEHM is performing well. There is some late-time disagreement; the FEHM solution under-predicts the water mass in the system. This discrepancy may be due to loose iteration criteria, some small and unidentified loss of water over the long simulation time, or another minor issue with the code. Otherwise we get a satisfactory fit between the two solutions.

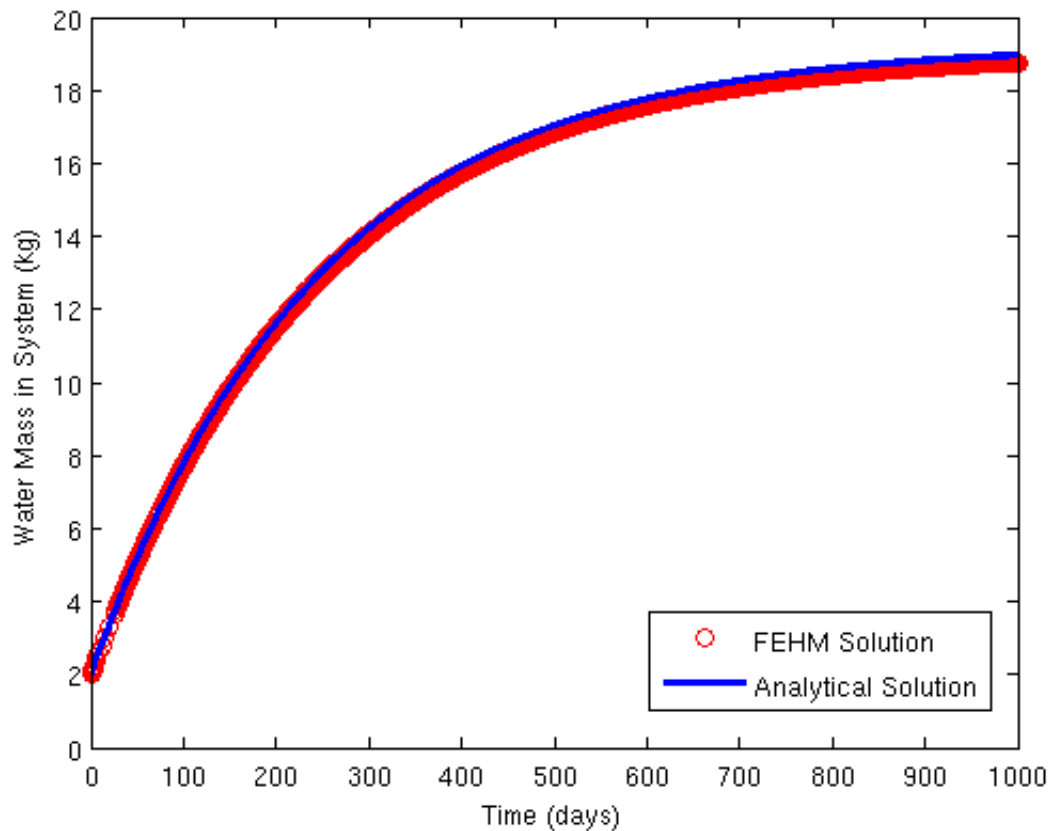


Figure 7: Comparison of FEHM results to the analytical solution for Test 2b.

3.2 Water vapor pressure

Water vapor pressure (P_{wv}) lowering due to dissolved salt in liquid water is an important process to accurately represent in simulations of gas and water flow in porous salt. P_{wv} can be thought of as the tendency of liquid water to turn to vapor. As this value approaches ambient (i.e. atmospheric) pressure, increasing amounts of water will go into the vapor phase. As temperatures increase the P_{wv} because the air has a greater capacity to hold water vapor at warmer temperatures; the temperature- P_{wv} relationship follows an exponential curve with P_{wv} increasing more rapidly as air warms. In contrast, increased solute concentration has the opposite effect. The addition of salt raises the boiling point of water and therefore lowers the P_{wv} of saline brine compared to equivalent pure water. P_{wv} for saline water can be rule-of-thumb estimated at about 75% of the P_{wv} for pure water when atmospheric air is fully saturated.

We constructed a test problem to determine if FEHM was properly calculating P_{wv} following code modifications to the routine `vaporl_salt.f`. The objective is to compare P_{wv} values from the code to estimated P_{wv} values for specified temperature and humidity. We show that pre-2016 code correctly calculated these values, but the early 2016 changes caused this to be incorrectly calculated. A code update released in June 2016 fixed these issues.

3.2.1 Grid parameters and model setup

The grid for this test problem is a 1-dimensional line of 10 nodes, each separated by 1 m (Figure 8). Temperature is specified at each node individually, increasing in the x-direction (Table 2). The salt module is enabled but no significant air flow, water flow, or salt motion is occurring. Porosity is specified at 0.3 with air and water vapor in each node. Output of interest is the P_{wv} for each node.

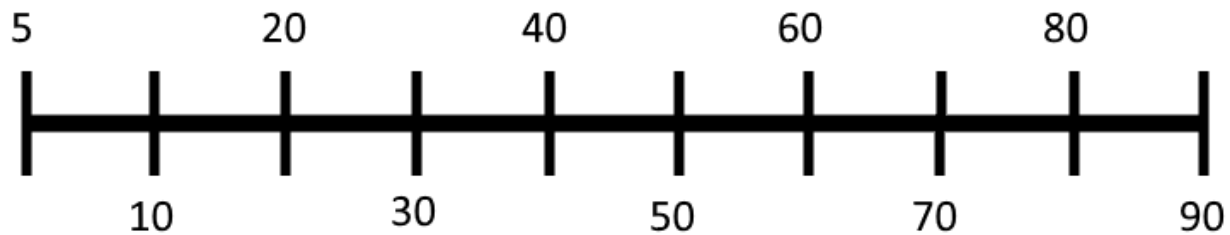


Figure 8: Model setup for P_{wv} test problem; numbers indicate temperature.

Table 2: x-distance vs. temperature specified at each node.

x (meters)	Temperature (°C)
0	5
1	10
2	20
3	30
4	40
5	50
6	60
7	70
8	80
9	90

3.2.2 Results

In non-saline environments with 100% relative humidity, P_{wv} should follow an exponential curve bounded by 0.611 kPa at $T = 0^\circ\text{C}$ and by atmospheric pressure (101 kPa) at $T = 100^\circ\text{C}$. Data of water vapor pressure and mixing ratios is sourced from the NOAA Air Resources Laboratory (<https://www.ready.noaa.gov/READYmoistcal.php>). Expected values of salt are estimated at 75% of the pure air value. Prior to early 2016, the model correctly predicted P_{wv} for brine near this 75% value; the early 2016 model contained an erroneous calculation of

this value that resulted in a major overestimation of low-temperature P_{wv} , underestimation of high-temperature P_{wv} , and a slight decrease from 20 to 60 °C (Figure 9).

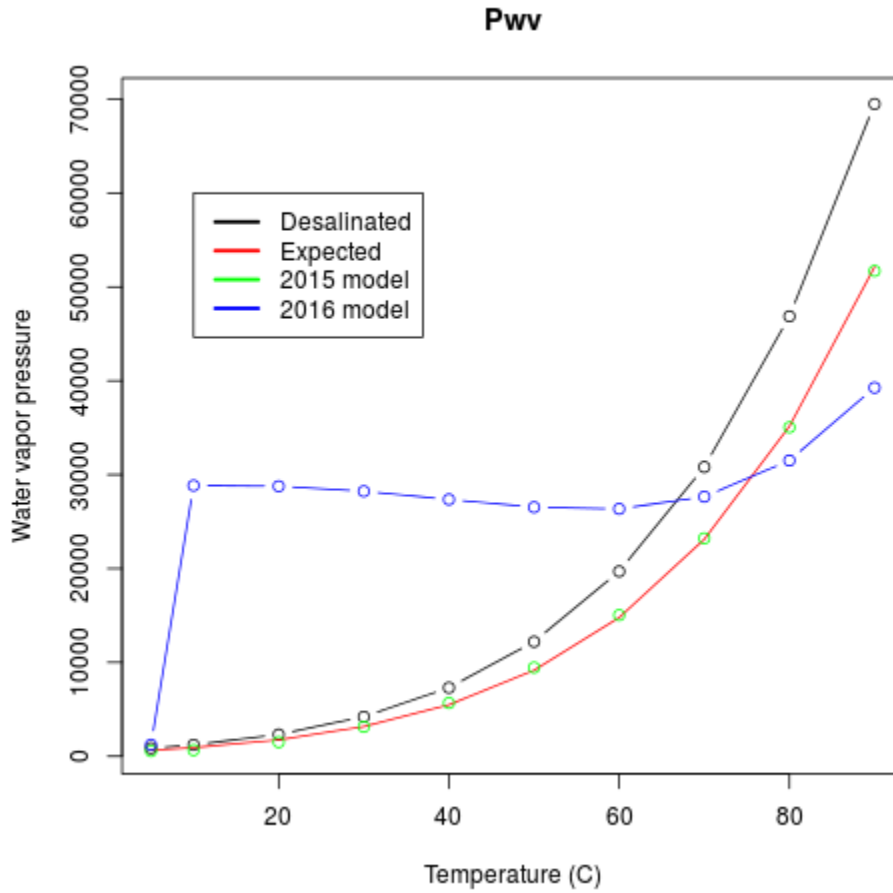


Figure 9: Desalinated water P_{wv} values (black), predicted 75% values (red line), 2015 model results (green), and early 2016 model results (blue), showing inaccurate P_{wv} values following amendments to `vaporl_salt.f`.

As of June 2016, a change has been applied to the salt code in the `vaporl_salt.f` routine. P_{wv} values following this correction are now in line with the 2015 model and fall near the expected ~75 % line (Figure 10). This example shows the need to include rigorous test problems that exercise a range of physics in the simulator. Such test problems can catch code bugs before they lead to problems in simulations and form the basis of QA on complex simulators such as FEHM, PFLOTRAN, and TOUGH2.

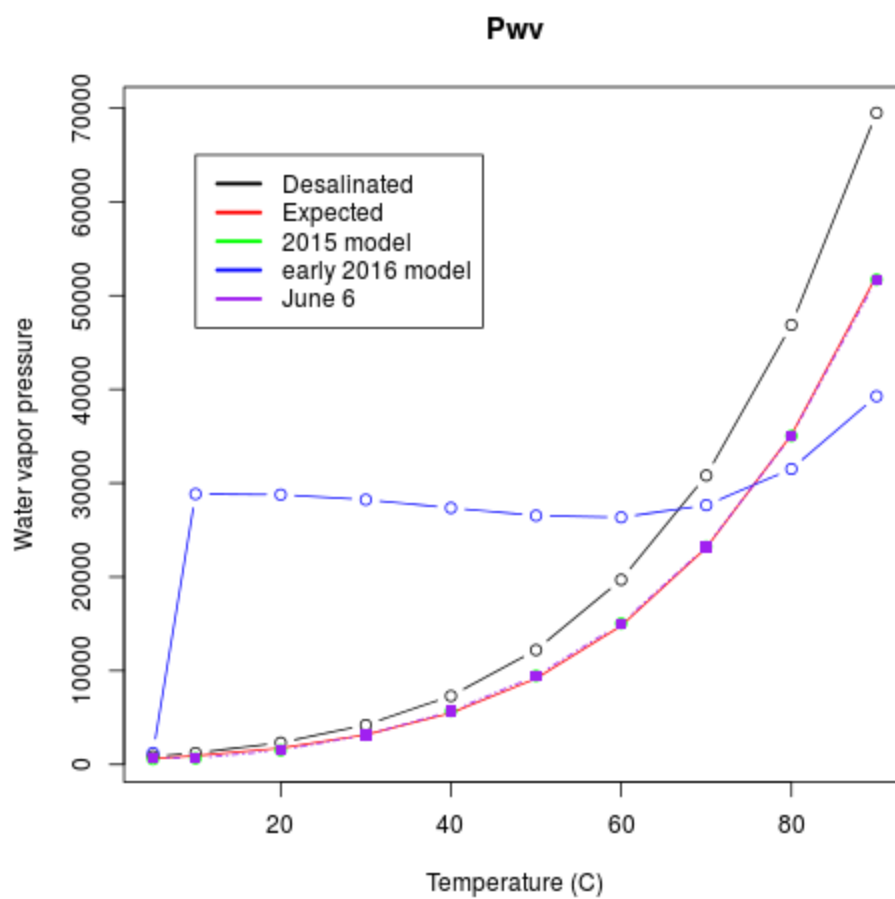


Figure 10: June 6 corrected values (purple) added to previous plot, showing corrected values after patch applied to vaporl_salt.f.

4 Olivella Experiment Modeling

4.1 Experiment description

Brine and mixed-phase migration of fluids in salt is important for understanding the self-sealing behavior of a salt repository (Kuhlman and Malamba, 2010). Experimental studies have demonstrated that porosity may migrate towards a thermal source for small-scale fluid inclusions within salt crystals (Caporuscio et al., 2013). However, in some conditions when pore space in salt is sufficiently connected for fluid migration to occur, porosity may be expected to migrate away from a heat source (Kelly, 1985). As saline water evaporates, salt concentrations increase until saturation is reached; as further water is removed, salt will begin to precipitate into void spaces previously occupied by water. Consequently, areas in which evaporation is occurring tend to be self-sealing, with reductions in porosity and permeability (Hansen and Leigh, 2012; Jordan et al., 2015c). Evaporated water, however, tends to condense as temperature decreases, resulting in dissolution of salt farther afield and increases in porosity and permeability. Previous experimental work (Olivella, 2011) was undertaken to examine this migration of porosity away from a heat source.

The Olivella et al. (2011) experiment used an insulated Plexiglas tube with a length of 10 cm and diameter of 5 cm (Figure 11) filled with crushed salt. One end of the tube was heated to 85 °C and the other end cooled to 5 °C. Measurements of porosity and brine content were taken at initial conditions and times of 7 days, 15 days, 30 days, and 65 days. This controlled experiment provides an excellent opportunity to test the new modules of FEHM against measured data.

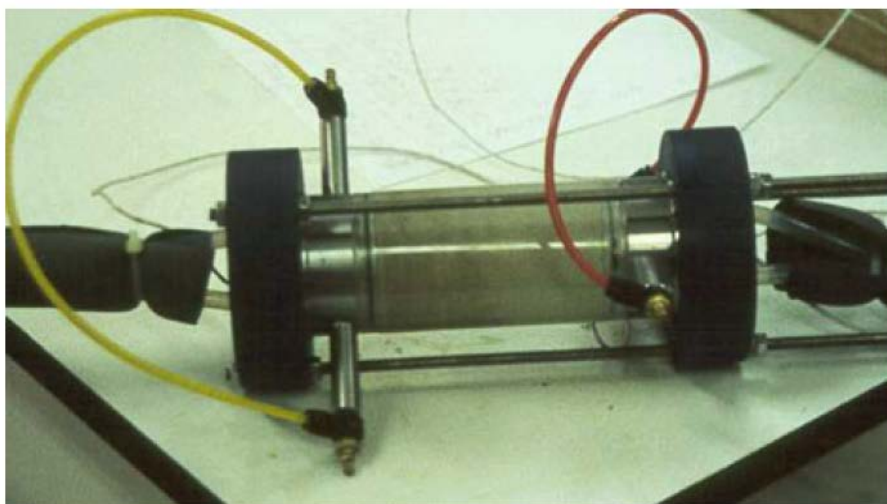


Figure 11: Experimental setup from Olivella et al. (2011).

4.1 First model test (no insulating layers)

For the first FEHM attempt, the salt module was applied to a 2-dimensional grid which had dimensions of 0.1 m length by 0.03 m width with 0.001 m increments. An 85 °C boundary condition was applied along the line of nodes at $x = 0$, and a 5 °C boundary condition at $x = 0.1$ (Figure 12). The model was run for 85 days, with results recorded at 7, 15, 30, and 65 days. Initial conditions placed the entire tube at 20°C and a temperature gradient was quickly reached over the 0.1 m salt canister. Resulting porosity profiles for each time period are shown for experimental results in Figure 13 for comparison with model results (Figure 14). Salt parameters are shown in (Table 3).



Figure 12: Model domain for case with no insulating layers.

Table 3: Salt properties used in modeling.

Property	Value	Units
Solid density	2165.0	kg/m ³
Specific heat capacity	931.0	J/kg·K
Permeability	1×10^{-12}	m ²
Thermal conductivity	2.0	W/m·K
Porosity	0.3	-
Initial saturation	0.4	-

Model results for this initial run appear to consistently overestimate the degree of pore closure near the heat source compared to the experiments. In addition, the location of increases in porosity are closer to the heat source in the model runs than in the physical experiments. Simulated results show the greatest porosity around 0.04 to 0.06 m from the heat source, suggesting this is where the greatest dissolution is occurring. Major increases in porosity on the

cool end of the salt canister observed in Olivella et al. (2011) which show dissolution increasing the porosity from 0.3 to 0.6 after 65 days (Figure 13). In contrast the simulated results show only a porosity change from 0.3 to 0.32 after 65 days (Figure 14). This discrepancy may be attributable to two factors: (1) differences in temperature gradients in the model versus the experiment, or (2) the present lack within the model of a capillary pressure function that would alter pressure gradients depending on porosity. The first of these is considered subsequently, while the second will be explored in future work.

The established temperature gradient of the model (Figure 15a) and the influence of temperature on specific humidity (Figure 15b) suggests that the most significant changes in porosity should be occurring where the changes in specific humidity are greatest. Because of the exponential nature of the relationship of temperature to vapor pressure, condensation of water and its consequent dissolution of salt occurs preferentially in steep segments of the T-Pwv curve (Figure 15b). Consequently, the model produces the largest changes around the point where temperature drops to 40-55°C. No temperature data was reported in Olivella et al. (2011), so it is possible that their temperature gradient was different than the model results. This could be the case if the cold side was warmer than previously reported, or if the limited heat passing through the insulating layers altered the temperature profile. Finally, our results are qualitatively similar to Runtqvist et al. (2016); however we have not been able to determine the conditions under which their TOUGH2 simulations caused porosity to increase preferentially at the 5C end of the simulation and mimic high porosity on the cold side of the experiment. These results do not agree with the underlying water vapor pressure function that suggests that most of the water diffusing toward the cold end should condense out by the 20C contour with little water left in the vapor phase to condense and create increased porosity at the fixed 5C end.

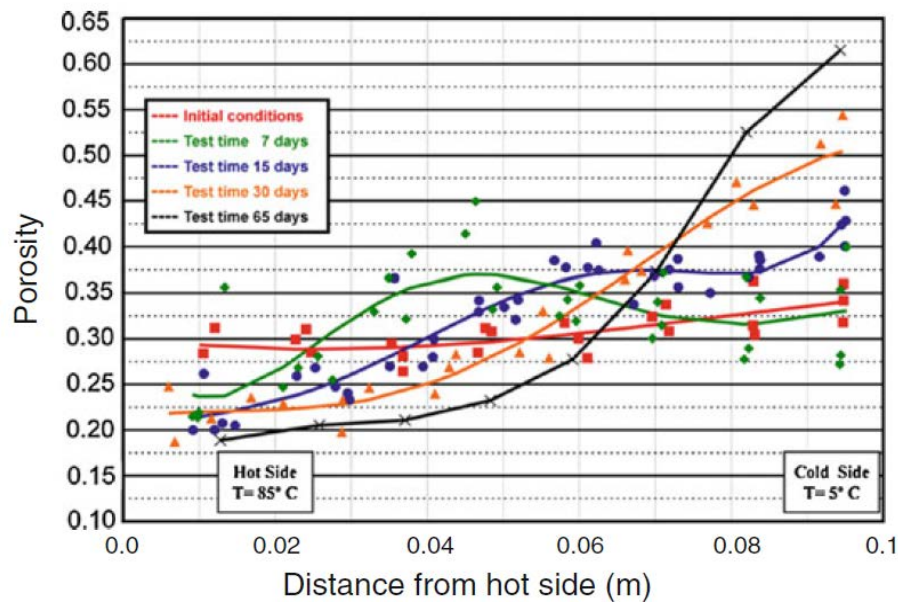


Figure 13: Observed salt tube porosity changes over time, from Olivella et al. (2011). Note the considerable increase at the low-temperature (right) side as time increases.

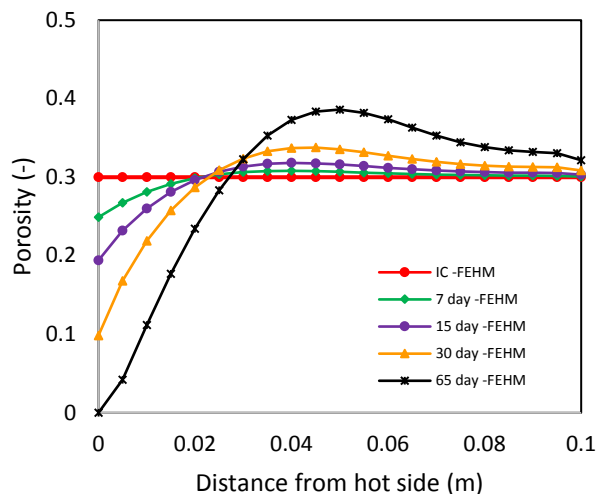
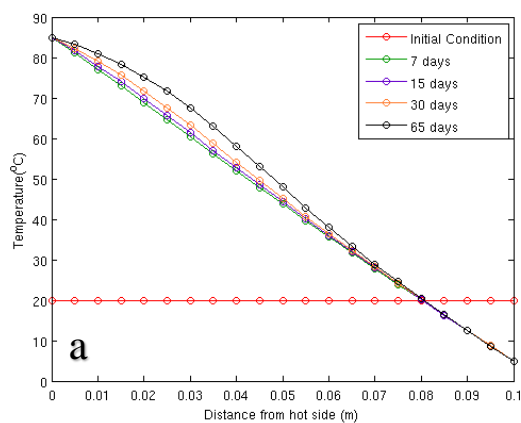


Figure 14: FEHM modeled porosity changes over time for a perfectly insulated salt tube. Porosity increases are primarily near the center of the tube.



Maximum Relative Humidity Curve

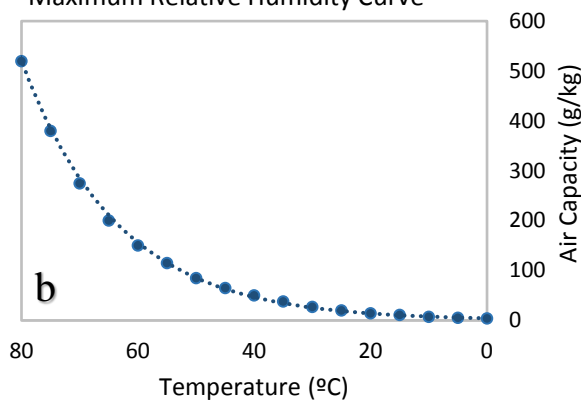


Figure 15: Temperature profile (a) and maximum relative humidity curve compared to temperature (b). Maximum relative humidity changes most rapidly above $T=50^{\circ}\text{C}$, so porosity changes would be expected to be most dominant in the warmer portion of the salt tube.

4.2 Second model test (with insulating layers)

To test the effect of insulating layers on the salt tube temperature profiles and porosity, a second grid was developed (Figure 16). This grid is rotated such that the heated side is at $y = 0$ and the cold side is at $y = 0.1$, with material properties changing in the increasing x -direction. This domain allows model runs to be conducted in a 2-D radial mode where node volume calculations are done in a cylindrical coordinate type approach; this allows investigation of model domains radiating outward from an interior point, instead of as 2-D slices of an infinitely long plane. Dimensions and material properties of the insulating materials were not quantified in Olivella et al. (2011), but were provided schematically without measurements. Materials in the insulators were listed only as “Sample ring (PVC),” “sealing rubber,” and a “plastic cover,” with no specifics given on what type of rubber or plastic were used. Consequently, thermal conductivity values were selected from a range of reported values from (Donalski and Hearing, 2016). Insulating units are assumed impermeable to water and therefore non-convecting. Thermal conductivity for each layer is assumed isotropic. Ambient room temperature was not listed by Olivella et al. (2011), and was therefore assumed at a normal room temperature value of 20°C . Insulator properties are shown in Table 4.

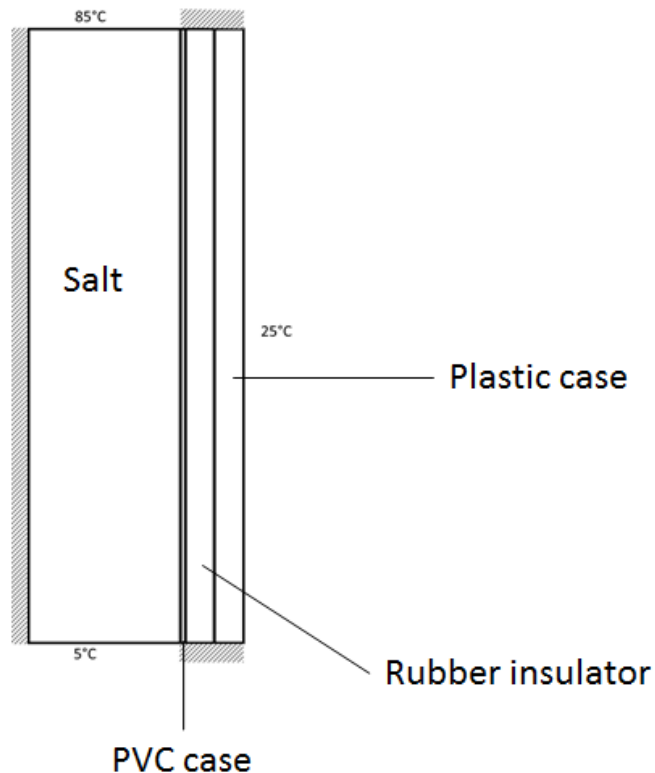
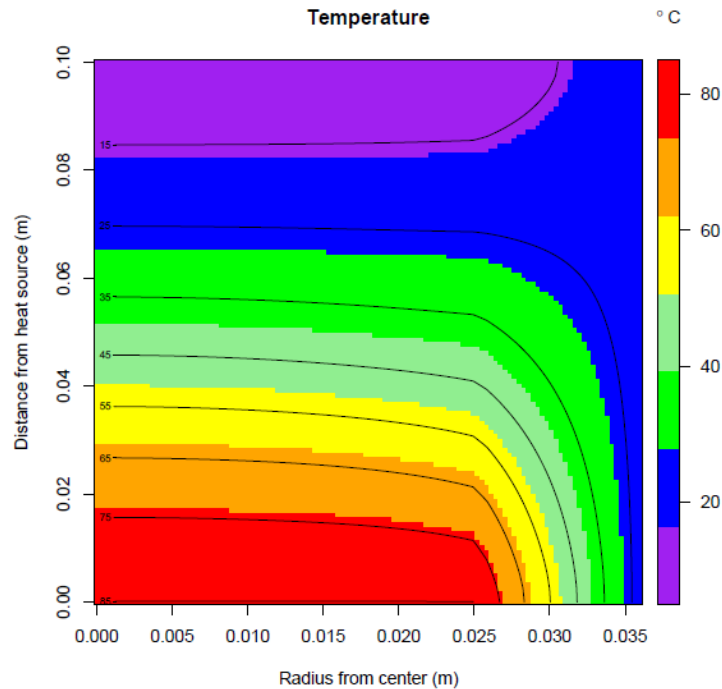


Figure 16: Model domain with insulated layers.

Table 4: Insulating layer properties.

Insulator	Thickness (cm)	Thermal conductivity (W/m · K)	Specific heat capacity (J/kg·K)
PVC	0.1	0.2	1000.0
Rubber	0.5	0.2	1100.0
Plastic	0.5	0.2	1670.0

With the addition of insulating layers, porosity and temperature form gradients that are affected laterally. Temperature contours (Figure 17) are slightly contracted towards the heater on the outward side as a low flux of energy passes through the insulating layers. Although this effect is minor in the temperature contours, it causes observable cross-sectional changes in porosity contours (Figure 18). An area of particular interest is the high porosity region abutted against the insulating PVC ring. This is likely the result of the slight depression of temperature gradients and spatially concentrated condensation of water causing dissolution of salt.

*Figure 17: Temperature contours with added insulating layers.*

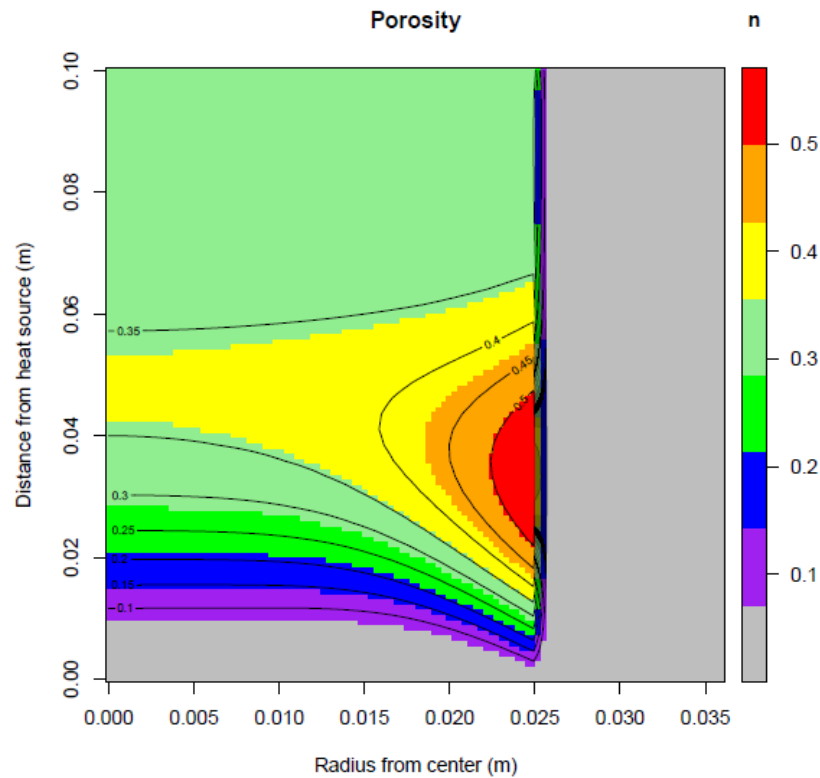


Figure 18: Porosity contours with added insulating layers.

The presence of the insulating layers causes a slight depression in centerline temperature towards the mid-section of the salt domain (Figure 19). As a result, long-term porosity changes (Figure 20a) are generally slightly depressed and shifted towards the heated side of the model domain. A slight increase in porosity relative to the no-insulator case is observed when insulators are added, but this effect is very minor compared to the original Olivella et al. (2011) results, wherein porosity near the cold side increased to 60 % by the end of the 65 day test period. Discrepancy between experimental results, model results, and anticipated conceptual results remains unresolved.

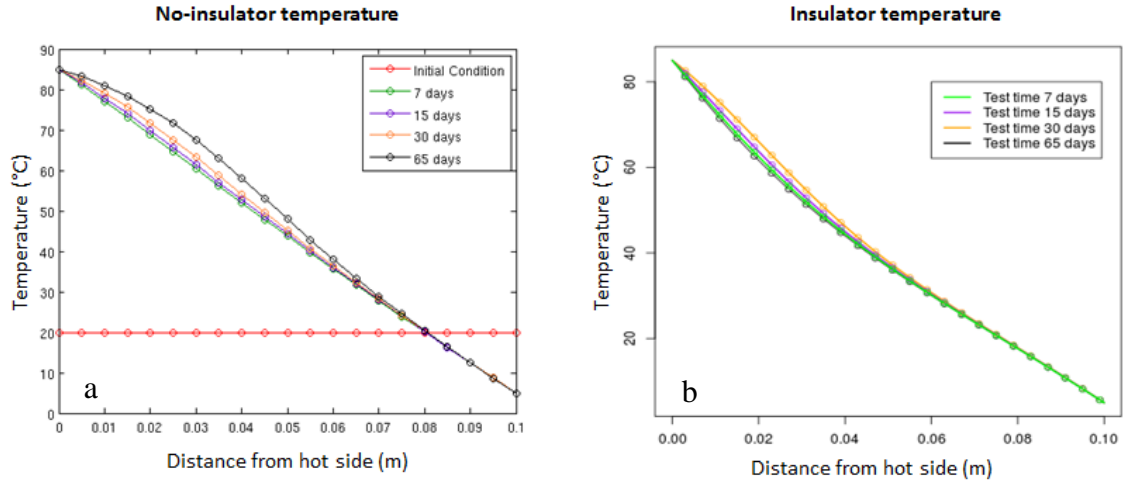


Figure 19: Temperature profiles for (a) simulations with no insulating layers (b) simulation including insulating layers. Discrepancies can be attributed to thermal conduction through insulating layers and minor differences in heat flow when porosity changes. Temperature profiles are notably depressed on the warm end in the insulated case.

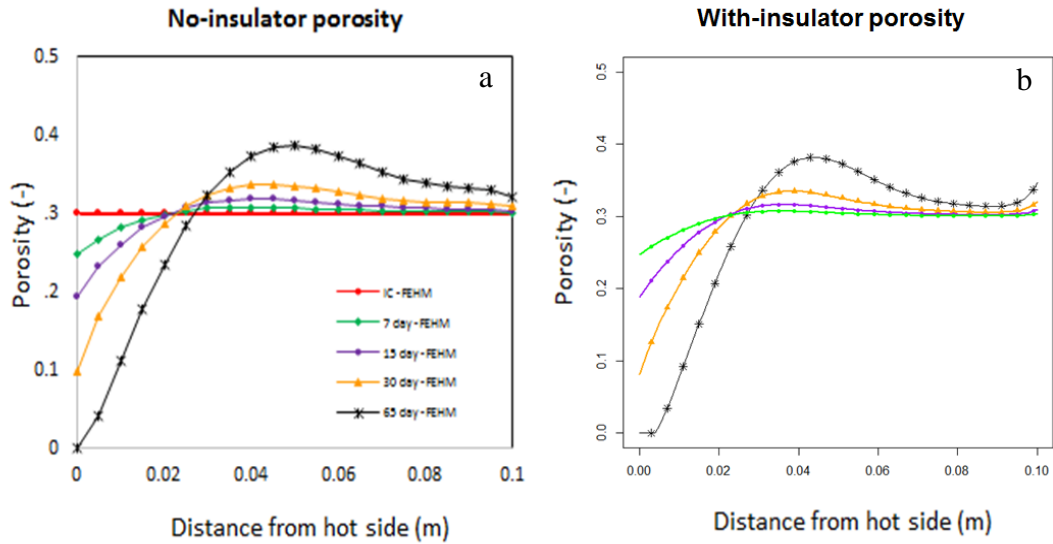


Figure 20: Differences in porosity in (a) no-insulator and (b) insulated cases. Center-domain porosities are comparable, but the case including insulators shows a slight increase at the cold end.

5 Pan evaporation experiment modeling

5.1 Experiment description

Building on the P_{wv} work described in Section 3, a topic of current interest is the vapor pressure (P_{wv}) lowering tendency of water with dissolved WIPP run-of-mine (ROM) salt compared to pure NaCl. Because of the impurities in ROM salt, it may be expected that water vapor pressure would be depressed even more than in pure salt (Figure 21). The added influence of salt on P_{wv} is important for retention characteristics of water within pores and the consequent dissolution and precipitation of salt in the presence of a thermal gradient. An experiment has been set up underground at WIPP in which run-of-mine salt was placed in a metal pan (Figure 22). Ambient temperature, humidity, and sample mass are measured continuously from May 2015 through May 2016. Changes in moisture content of the salt are interpreted from the change in mass at each measurement.

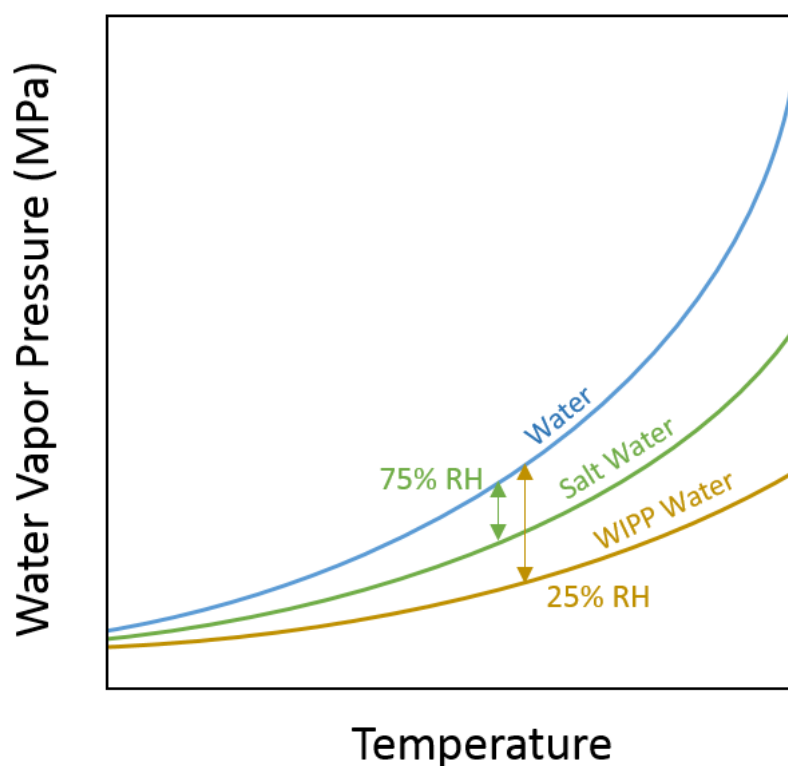


Figure 21: Conceptual model of water vapor pressure for desalinated water (blue), water containing NaCl salt (green), and water containing WIPP salt with impurities (yellow); salt and impurities depress water vapor pressure.



Figure 22: Salt pan experiment in WIPP salt gallery. Pans with salt piles are on left.

5.2 Model setup

Modeling of the WIPP salt pan experiment is on a 2-dimensional 30 by 30 cm square grid (Figure 23). Salt and air zones are defined; salt properties are as described in Table 3: Salt properties used in modeling above. To represent the changing humidity boundary condition, the macro control statement *fxa* was used. This statement applies a user-specified mixing ratio of air mass to water vapor mass. Atmospheric air at 29 °C and 100 % relative humidity contains about 25.42 grams of water per kilogram of air, for a water-air mass ratio of about 0.0284. For the *fxa* control statement the corresponding input would be $(1 - 0.0284)$ or 0.9716. Hence, as the *fxa* value approaches 1, air is progressively drier, and as *fxa* approaches 0 the gas phase becomes increasingly dominated by water vapor. The input values in this statement apply to inflow of air to the system and therefore require simulation of flowing air. To accommodate this in the model, a pressure change of 10^{-5} MPa (10 Pa) over 30 cm was applied with a slight inflow of air directly above the peak of the cone and a slight outflow of air directly above the low point at coordinates (30, 0.3) cm. A low flux of air with the desired water vapor mixing ratio would pass across the top of the salt cone and add or subtract pore water based on proportional water content of the air and salt.

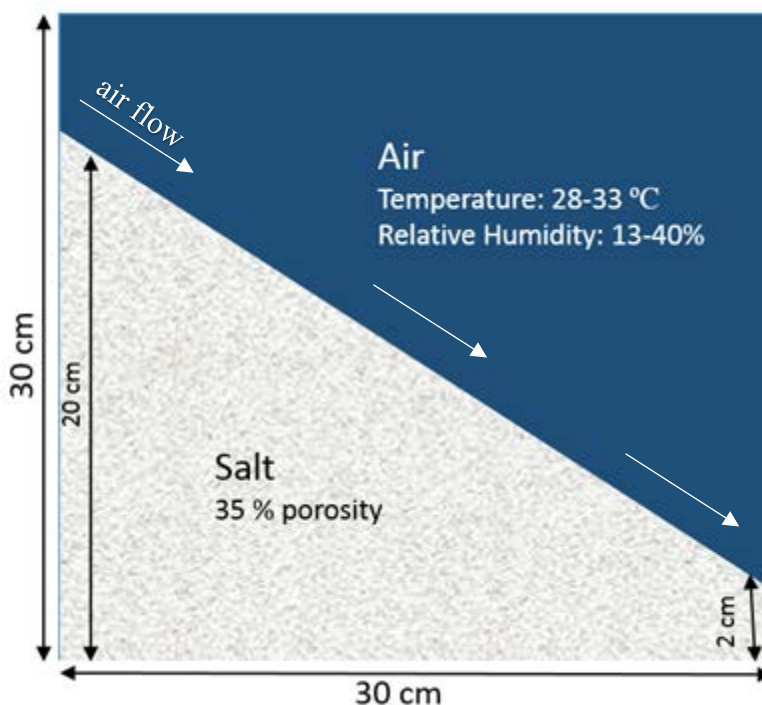


Figure 23: Model domain for salt pan experiment.

5.3 fxa test runs

In order to demonstrate the efficacy of the fxa macro, two simulation were run to test behavior in response to relative humidity end-members. fxa values of 0.9999 and 0.0001 (very dry air and essentially pure water vapor, respectively) were tested to ensure that humidity in the salt would properly change under these conditions. Model time periods for these test runs were 0.1 days, which is an adequate period to determine if saturation behavior is correct. Initial saturation started at 0.03. For the dry air volume fraction, saturation near the top boundary of the pile dropped from 0.03 to 0.00018, while the lower portions of the model stayed approximately constant. Relative lack of change can be accounted for by water retention at depth in the porous salt. Conversely, for the fxa run of 0.0001 with almost entirely water vapor, the pile reached full saturation within 0.1 days. Both of these test runs worked properly.

5.4 Test of fxa with air flow

A 12-day model run was conducted using laboratory-measured temperature and humidity conditions. As with the end-member runs described in Section 5.3, a minimal gas flux was induced across the top of the salt pile, with inflow air having temperature and water volume fraction values measured in the subsurface at the WIPP site. A background run was conducted first to reach a steady-state, initial condition for subsequent simulations. Mass changes of the simulated salt cone are compared to measured mass changes in the bench-scale experiment in

Figure 24. Due to uncertainty in the exact dimensions of the salt cone, mass changes were normalized to the percentage change of the total mass. Directionality of the modeled changes tracks well with measured values, with peak and valley inflection points correlating well. This shows that in situations with airflow with the *fxa* boundary applied, FEHM produces accurate values if humidity, air flow, and initial conditions are well established.

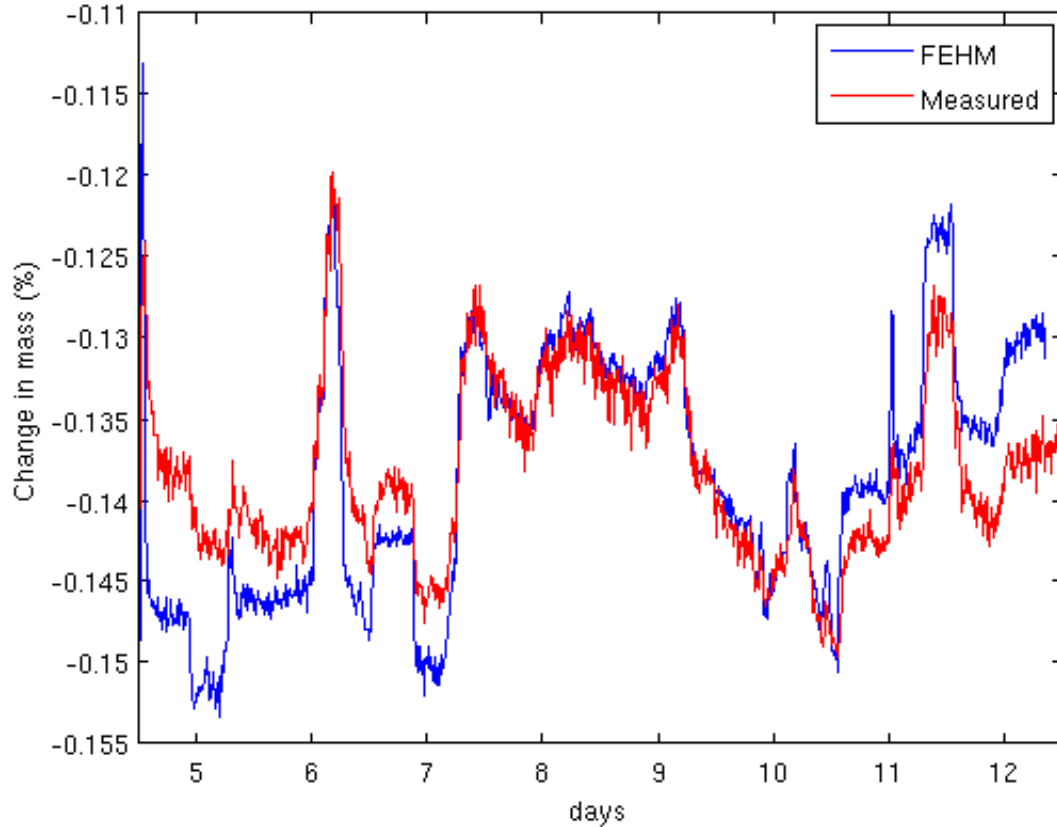


Figure 24: Mass change (%) of salt cone, showing comparison of FEHM model results (blue) to lab measurements (red).

6 Brine Transport Experiments in RoM Salt

6.1 Introduction

Bench-scale experiments performed this year build on the lessons learned and open questions from previous years' experiments. In our previous report (*Jordan et al., 2015a*) we performed several experiments specifically designed to map the 3D heat envelope developed in salt as a result of using a variable thermal output block heater. We also examined water vapor migration under conditions of varying temperature and airflow, and examined the extent of salt reconsolidation driven by salt dissolution and precipitation. The experiments were performed using commercial granular sodium chloride salt with an average grain size of about 2 mm. The

moisture content of the salt was fixed at 2.0 weight percent by adding saturated brine to the bottom of the salt pile. We found that the hygroscopic behavior of the salt played a significant role in water vapor migration. The results suggested that RoM salt which contains accessory minerals with strong water absorption properties would have an even stronger influence on water vapor transport through the salt. We also tested the diffusion of multiples tracers to interrogate internal structural changes in the salt as a result of heating and water vapor flow. Our data showed that over the course of 3 weeks, breakthrough curves for chloroform and SF₆ (a non-interacting tracer) became significantly more delayed, requiring smaller effective tortuosities to fit the data with a simple analytical solution to the advection-dispersion equation, suggesting an increase in salt reconsolidation which was verified through post-test forensics. Results from the final experiment showed strong indications of vapor-liquid cycling and salt dissolution and precipitation. These significant changes in the salt were driven by the abundant brine available in the salt pile. The results from these examinations were very informative and instrumental in building a robust experimental setup that provided useful data for model validation. However, the granular salt lacks the complexity of RoM salt which typically has lower moisture content, a higher grain size, and contains accessory minerals at about 0.5-1 wt.%. The impurities in salt and the lower moisture content are likely to limit the extent of water vapor transport and salt dissolution and reconsolidation processes. In order to confirm these predictions and to provide data for model validation, we performed a series of heating and cooling experiments in the same salt enclosure used in the previous studies with RoM salt. The RoM salt used in our experiments was obtained from the (WIPP).

In the current report we describe a series of heating and cooling experiments performed in an enclosure filled with RoM salt designed to refine the model prediction of temperature propagation in a salt pile and to reduce uncertainties in the behavior of brine, water vapor, and solid salt reconsolidation in the vicinity of a heat generating source. The experimental data obtained from this work which consist of 3-D, spatial representation of temperatures in heated salt, and water vapor transport will help improve the numerical representation of the coupled thermal, hydrological, mechanical, processes in salt. Even though the experiments were performed with RoM salt obtained from WIPP, the results from this research is likely to fill science gaps that apply to any potential salt HGNW repository setting (*Robinson et al.*, 2012).

6.1.1 Objectives

This work is a continuation of the effort started in 2015 and summarized in our progress report (*Jordan et al.*, 2015a). The objectives of this work are to: (1) develop an understanding of the specific physicochemical processes that may operate during disposal of HGNW in drifts or alcoves with backfilled rubblized salt (RoM salt), and during full-scale heater experiments, that can be observed under controlled conditions in the laboratory; and (2) validate numerical models that attempt to represent changes in salt structure and associated flow and transport processes.

6.1.2 Background

Several documents are available with detailed descriptions of previous studies that focused on coupling thermal, hydrological, mechanical, processes in salt ((*Hansen and Leigh*, 2011, *Pollock et al.*, 1986; *Rutqvist et al.*, 2005; *Bodvarsson et al.*, 1999, *Robinson et al.*, 2012, *Caporuscio et al.*, 2013, *Stauffer et al.*, 2013, *Stauffer et al.*, 2015, *Jordan et al.*, 2015a). Heat generating high level waste contains fission products such as Cs-137, Sr-90 which have short lives and are mostly responsible for the heat load of the waste packages. When emplaced in salt the HGNW will create a heat gradient with temperature difference between hot salt (in contact with the heat source) and ambient salt (sufficiently far to remain cool) of about 100 °C. This temperature gradient will induce air and moisture flows especially in crushed RoM salt material used as backfill over the waste canisters. From *Jordan et al.*, 2015a

“Temperatures around the waste may exceed the boiling point of brine, and if conditions are conducive to it, a heat pipe may be established in the crushed salt backfill (Figure 25). In a heat pipe, water is vaporized in the boiling region, advects and diffuses along concentration gradients to the cooler regions where it condenses, and replenishment of fluid towards the heat source is established from gravity flow and capillary pressure gradients (*Doughty and Pruess*, 1990). Water sources in the system that may feed the heat pipe include free pore fluids in the RoM salt, inflow from the DRZ into the RoM backfill, release of water from hydrous minerals, and, potentially, fluid inclusion migration up a temperature gradient. If a heat pipe is established, the result is a higher apparent or effective thermal conductivity and flatter temperature gradients around the waste (*Birkholzer*, 2004), lower maximum temperatures, and buildup of a low-porosity rind from evaporating brine in the boiling region (*Stauffer et al.*, 2013). “

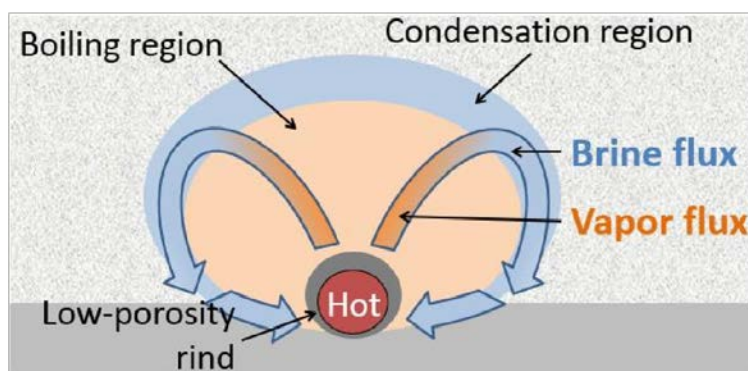


Figure 25: Heat pipe in salt. (from *Jordan et al.*, 2015a)

While our previous examination of these processes in granular salt showed strong evidences that water vapor transport and significant salt consolidation around the heat source occur, it was not known if such processes will be as significant in RoM dry crushed salt backfill. The hygroscopic properties of the accessory minerals present in salt could completely stop or limit moisture vapor transport and therefore limit the extent of salt reconsolidation. There are no data in the literature that specifically examine coupling between a heat source heat load, moisture content, accessory mineral content and salt reconsolidation properties. Some preliminary laboratory and in-situ testing of evaporation from granular salt performed by our

team (*Shawn Otto and Doug Weaver*) does suggest that underground salt at WIPP plays an important role in modulating the relative humidity of the air that circulates through the repository. These data suggest that moisture retention properties of the salt which is related to its content in accessory minerals is likely to be critical to the reactivity of heated salt. In this work we specifically focused on vapor transport and reconsolidation in a heated dry granular RoM salt.

6.2 Experimental method

6.2.1 Salt box setup

We used the same experimental setup described in our 2015 progress report (*Jordan et al., 2015a*) except that the enclosure was filled with RoM salt obtained from WIPP. The enclosure consisted of a 2 ft by 2 ft by 2 ft Plexiglas box, 0.5 in thick, with a removable lid, filled with RoM salt. The setup is shown in Figure 26.

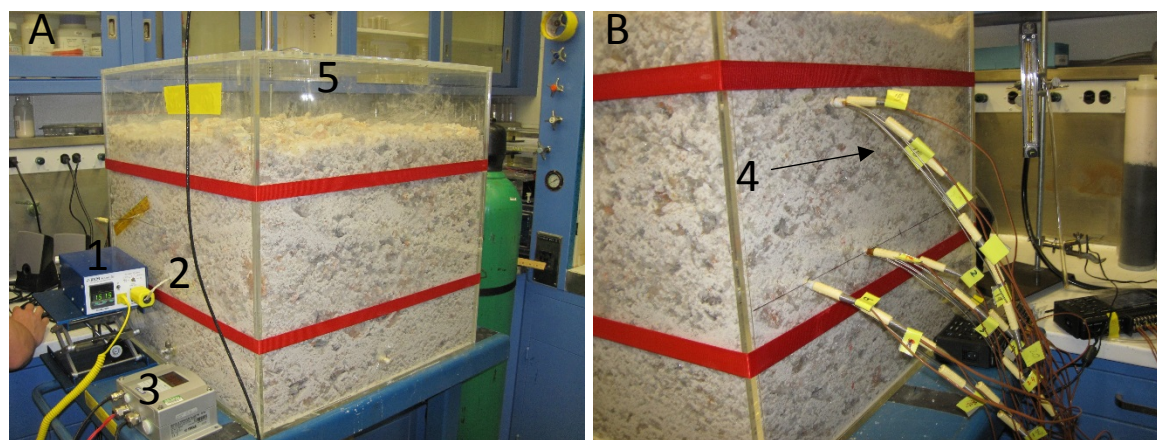
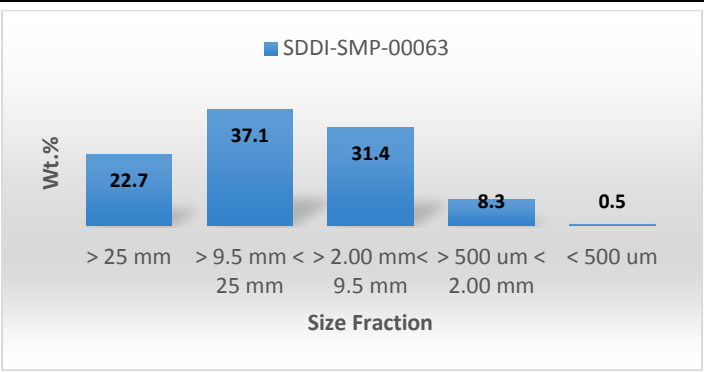


Figure 26: Pictures A and B show a salt enclosure (salt box) filled with RoM salt used in our experiments. (1) Temperature controller, (2) heating black power supply, (3) RH logger, (4) thermocouple bundle, (5) Plexiglas enclosure.

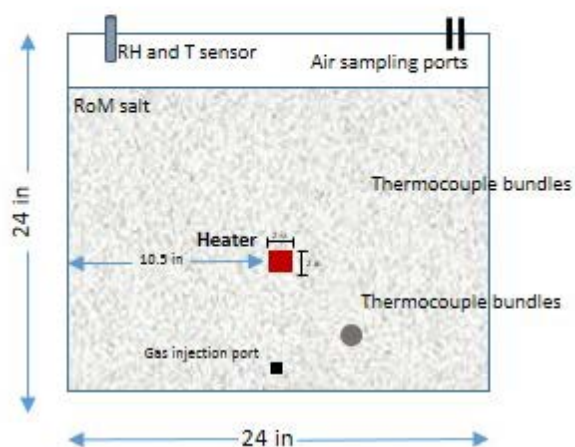
The enclosure was filled with 500 ± 20 lb of salt obtained from WIPP. The salt was packaged underground in sealed individual buckets that weighed about 50 lb. The packaged salt was stored under ambient conditions in sealed buckets until used. The salt was poured directly in the enclosure and leveled by hand without any sorting. The porosity of the salt, its size distribution, and accessory minerals content were determined on subsamples from a RoM salt shipment received in 2013. The moisture content was determined by averaging moisture content for 10 subsamples taken from different buckets of the salt used in this experiment. The different properties of the salt enclosure are summarized in the Table 5.

Table 5: Properties of the bulk RoM salt used in the experiments.

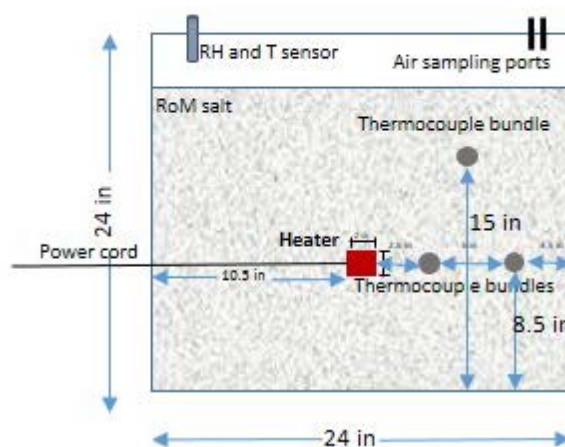
	Constant	Value	
Size distribution		 <p>■ SDDI-SMP-00063</p> <p>Wt. %</p> <p>22.7 37.1 31.4 8.3 0.5</p> <p>> 25 mm > 9.5 mm < 25 mm > 2.00 mm < 9.5 mm > 500 um < 2.00 mm < 500 um</p> <p>Size Fraction</p>	
Moisture content		0.19 ± 0.03	
Accessory minerals content		0.44 ± 0.1 wt. %	
Porosity	ϕ	0.39 ± 0.1	
Bulk	Density, ρ (g/mL) ^d	1.2	
	Specific heat, c_p (J/kg-K) ^e	927	
	Thermal conductivity, K_t (W/m-K) ^f	25°C	250°C
		0.84	0.45

The salt box was instrumented with a heater block powered by a temperature controller that maintained the heater at a fixed temperature. The aluminum heater block (2 in. wide by 5 in. long and 2 in. high) was set at about the center of the salt box. Its exact location is depicted in Figure 27. The temperature distribution in the salt was recorded using 20 individual thermocouples spatially positioned to capture temperature profiles in a quarter-space of the salt box. The thermocouples were positioned in bundles set parallel to the heating source. Individual thermocouples were separated by 2 inches from each other (see Figure 27). A data logger was used to record the temperature readings. A Vaisala relative humidity probe (model HMT 330) was also used to measure the relative humidity and temperature in the air gap of the box.

Side View 1



Side View 2



Plan View

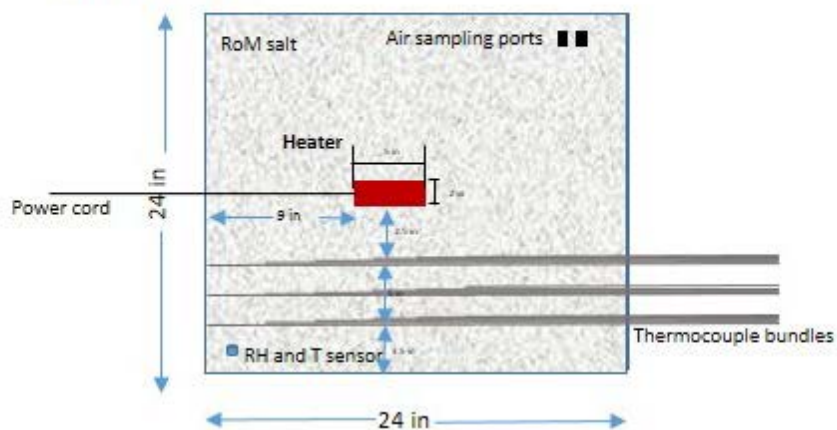


Figure 27: Schematic representation of a salt box filled with RoM salt and instrumented with a heater thermocouples a relative humidity probe and gas sampling and injection ports.

Table 6: Summary of the specifics of the salt box used in the experiments.

Object	Dimensions/Locations/properties
Box	Outer dimensions L x W x H= 24 x 24 x 24 in
Heat source	L x W x H = 5 x 2 x 2
Heat source position within the salt box	11 inches from the bottom and 9 inches from the front wall
Salt amount and height in the box	19 inches above the base
Thermocouples placements	3 bundles with a total of 20 point reading distances from the heat source are shown in Figure 27
Tracer used	SF6 and chloroform
Salt used and properties	WIPP RoM salt Moisture content 0.19 wt. % Amount of salt used 500 ± 20 pounds Porosity of salt 39% Accessory minerals content 0.44 %

6.2.2 Temperature profile mapping

Several heating and cooling experiments were performed in the salt box to capture the heat envelope developed within the salt pile. All experiments were performed by fixing the temperature of the heating block to the desired temperature and monitoring the temperature readings of the different thermocouples until they reached a steady state. The temperatures selected for our experiments were 50 °C, 100 °C, 150 °C, 200 °C, and 250 °C. For all temperatures studied the heating block stabilized at the set temperature within a few minutes. However, the temperature in the salt surrounding the heated block took much longer to stabilize. When steady state temperature were reached the heaters power was turned off and the salt in the box was allowed to return back to ambient temperature before the heater was set to a new temperature. In addition to temperature recording, we continually monitored the relative humidity and temperature in the air gap above the salt and the temperature at several location on the outside surface of the salt box (Figure 28).



Figure 28: Infrared imaging of salt box at maximum temperature of 260 °C.

6.2.3 Tracer injections

Prior to performing the heating and cooling experiments, we monitored the relative humidity in the air gap above the salt box at ambient temperature. The salt box was completely sealed; no air exchange with the outside was allowed. The relative humidity reading stabilized very rapidly and only varied slightly between the day and night cycles. A tracer transport experiment was also performed to characterize the initial state of the box. The experiment was performed by injecting a small volume of a mixture of sulfur hexafluoride (SF_6) and chloroform (CHCl_3) through the injection port, which consisted of a valve equipped with a septum and a thin stainless steel tube that extends to the center bottom of the box. The air gap above the salt was sampled continuously for tracer gases analysis. The sampled gas was recirculated back to the air gap so that there is no net loss of tracers from the enclosure. The flow rate of air sampling was fixed by the gas analyzer. The gas analyzer used was a Bruel & Kjaer photo-acoustic multi-gas monitor which non-destructively analyses multiples gases. The tracer gases – chloroform (CHCl_3) and SF_6 – were chosen because the multi-gas monitor can measure those two gases to sub ppm concentrations. SF_6 is a conservative tracer and is thus a non-interacting gas diffusion through the salt (negligibly partitioning). Conversely, chloroform does partition in water and was chosen to be a good indicator of moisture content of the salt. The gas mixture was formulated by pipetting 1.0 mL of liquid chloroform into collapsed 140 mL plastic syringe and expanding the volume of the syringe to 120 mL using SF_6 . Chloroform vaporized rapidly to create a homogeneous gas mixture. Tracer injections consisted of injecting 40 mL of the gas mixture into the injection port. The tracer pulse injection typically takes about ten seconds.

Tracer experiments were also performed after powering the heater block to 80 °C, 160 °C, and 260 °C. Tracer experiments were performed immediately after the heater temperature stabilized to the set temperature and several days after the salt box had reached steady state temperature conditions.

6.2.4 Post heating forensics - Salt dissolution and re-precipitation in sea salt experiment

A detailed, post-heating forensic examination was performed by excavating the salt packed in the salt box to complete the work reported in FY15 progress report. This was done to complete the experimental work performed using uniform salt (NaCl) of approximately 2 mm and heated to a maximum of 260 °C. The initial porosity was 35 % and the moisture content was 2.0 wt.% ponded saturated brine injected at the bottom of the tank. The experiment was designed to identify the structural changes in salt that induced the significant permeability changes reported in our FY-15 progress report (*Jordan et al., 2015a*). Discrete samples were collected with depth at different locations in the salt pile and petrographic thin sections were made by embedding the salt in an epoxy resin and polishing it to 30 um. The thin sections were analyzed using a petrographic microscope and processed numerically using Photoshop to quantify their porosity.

6.3 Results and Discussion

6.3.1 Temperature profile in RoM salt experimental data and modeling

Heating experiments show a rapid exponential increase in the salt temperature at a given distance from the heat source followed by a slow steady temperature rise toward the steady state. This behavior is indicative of slow changes in the heat conductive properties of the salt. Such behavior is likely the result of a slow and steady increase of the moisture in the air pockets present in the pore space between the salt grains, therefore making the air pores the overall material more conductive (Figure 29). This is in contrast with the experiments performed in granular salt for which the temperature increase profile is much smoother (Figure 6, *Jordan et al., 2015a*). This behavior is observed at all temperatures as is indicated by the plot in Figure 29.

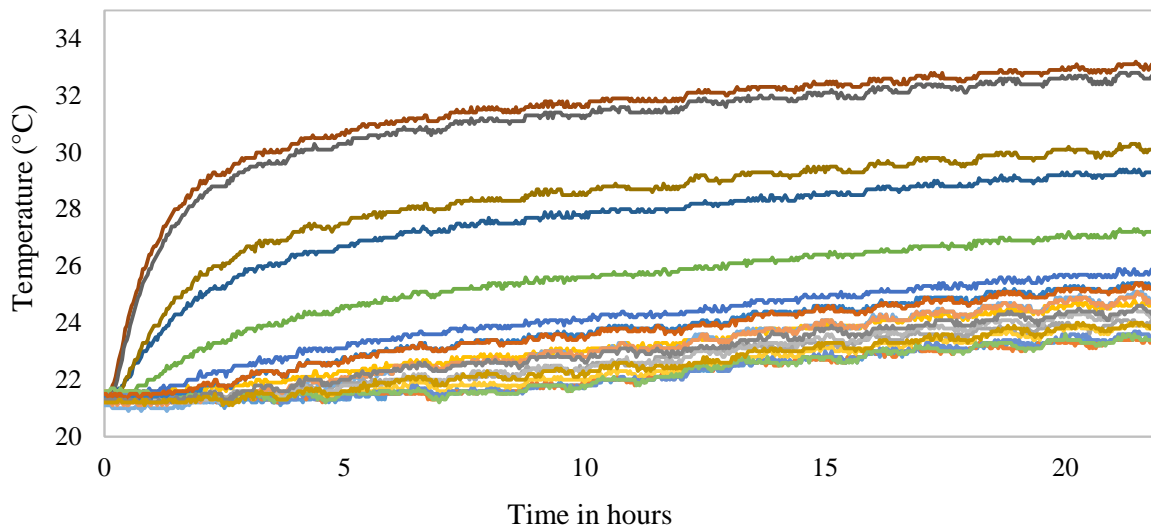


Figure 29: Temperature profile with time for the thermocouples placed at different distances from the heat source. The heating block was set at 50 °C and the closest thermocouple (highest temperatures) was set at 6.35 cm from the heater.

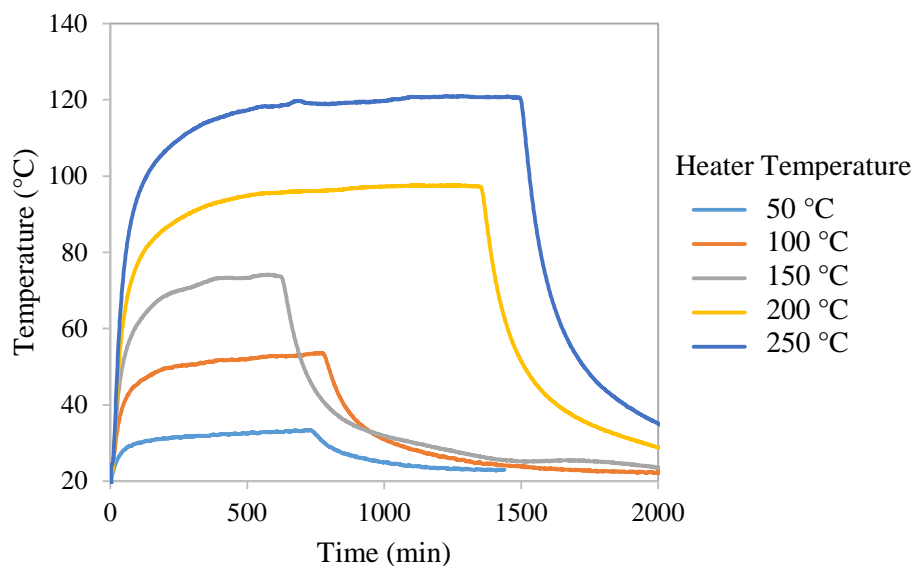


Figure 30: Temperature profiles at a set point 2.5 inches from the heat source. The heat source temperature was fixed at the indicated temperatures using a temperature controller and was turned off after temperature of the salt reached a steady state and let cool down to ambient temperature.

The conductivity of the salt is quite low as evident by the very rapid decrease of the temperature away from the heat source (Figure 31). The plot shows the temperature decays as a function of the distance from the heat source for experiments at 50, 100, 150, 200, and 250 °C.

After the temperatures reach equilibrium the cooling and reheating of the salt results in very similar profiles indicating very little changes in the salt heat conductive properties. This drop in temperature with the distance is not predicted well by the thermal conductivity function currently developed for the BAMBUSII experiments (Bechtold et al., 2004). During the BAMBUSII experiment, a thermal conductivity relationship of RoM salt was determined from field experiments for drift and back-filled salt at a German salt mine. This relationship is porosity and temperature dependent and is described by Equations 3 and 4 and shown in Figure 32. The BAMBUSII function is empirical and includes a fitting factor, which suggests that the thermal conductivity may be useful only for the site for which it was determined and not applicable to WIPP. Factors, such as water content or impurities in the salt may result in very different thermal properties of different salt deposits.

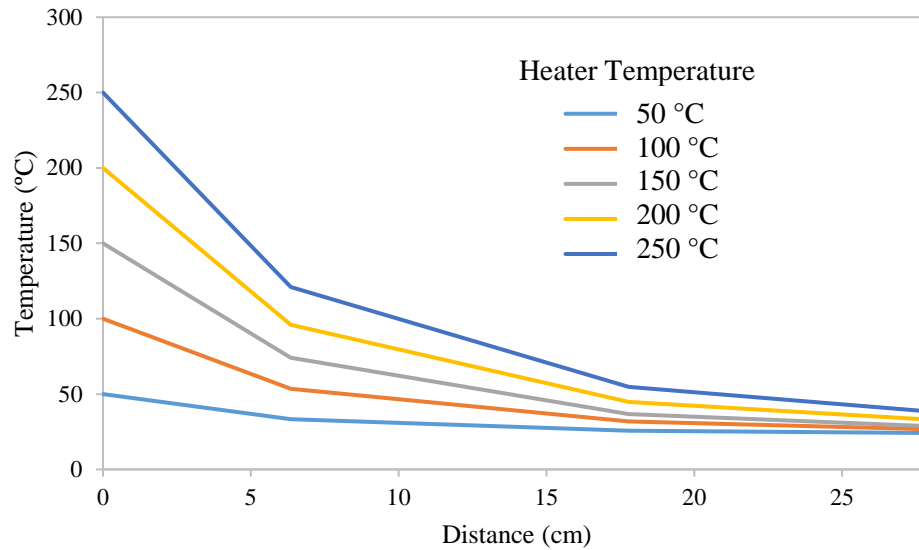


Figure 31: Temperature distribution in a RoM salt as a function of the distance from the heat source. The different lines represent independent runs performed by fixing the temperature of the heat source to the indicated temperatures.

$$k_{cs}(\phi) = (-270\phi^4 + 370\phi^3 + 136\phi^2 + 1.5\phi + 5) \cdot f \quad \text{Equation 3}$$

$$k_{c-salt}(T) = k_{cs}(\phi) \left(\frac{300}{T} \right)^\gamma \quad \text{Equation 4}$$

k_{cs} = thermal conductivity (crushed salt), ϕ = porosity, f = fitting factor, T = temperature, γ = material constant

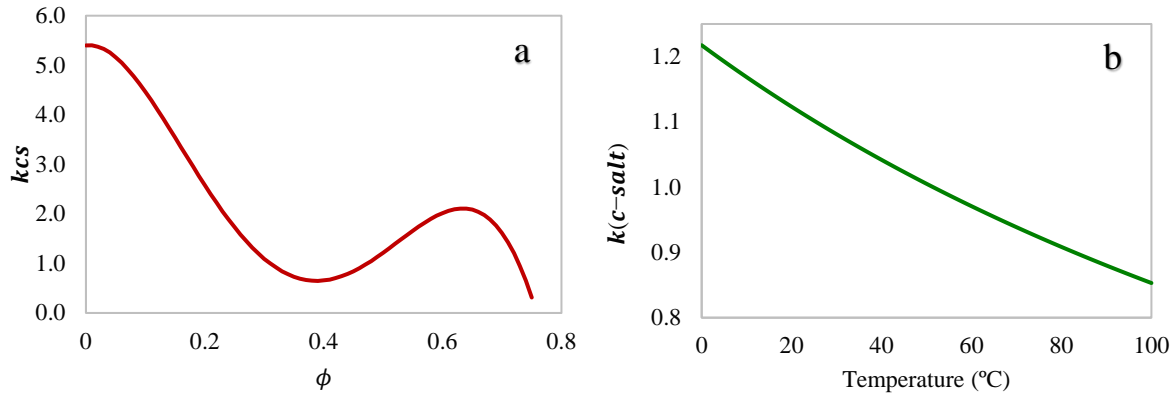


Figure 32: Thermal conductivity of RoM salt based on the BAMBUSII experiments. (a) shows thermal conductivity dependence on porosity (Equation 3) and (b) shows a thermal conductivity curve changing with temperature for salt with porosity = 0.3 (Equation 4).

To test if the BAMBUSII thermal conductivity relationship is appropriate for WIPP salt, the functions (Equations 3 and 4) were added to the salt module of FEHM and the heater block experiments were modeled. The model uses the same grid and dimensions as described in the Jordan et al., 2015a (Figure 7 and Table 2), but with minor modification to reproduce the conditions of the current experiment. Initial modeling of the experiment show that the BAMBUSII relationship of thermal conductivity may not be an accurate method for estimating the thermal conductivity of RoM salt at WIPP. The modeled temperature results at the thermocouple locations are compared to the temperature measurement for a bench top experiment in Figure 33. For all simulated cases we see a poor fit between the simulated steady-state temperatures to the measured data near the heat source, where temperature is changing the most dramatically. We also see that the BAMBUSII relationship used in the simulations does not consistently over- or under-predict the temperature response depending on the heater block temperature. The 80 °C simulation tends to under-predict heat conduction across the domain, while the 260 °C simulation tends to over-predict the heat conduction. However, there is a fairly tight fit for the 160 °C case, especially in the region of 30-50 °C. We attribute these differences to several parameters tightly linked to the specific nature of the salt used in our experiments which includes, variable pore size distribution resulting from the inhomogeneous grain size distribution of the RoM salt (see Table 5), the presence of accessory minerals such as clay with lower thermal conductivity, and water which is also less conductive than salt. There is also a poor coupling between salt and the heating block which results in an immediate drop of the temperature at the surface of the salt that comes in immediate contact with the heater. Some of this drop is also attributed to the bigger air gap that is established between the salt layer and the flat surface of the heater which is significantly less conductive. These results and considerations suggest that the differences between the impurities in the salt at the BAMBUSII site and WIPP cause large enough variations in the thermal conductivity of the material to significantly change thermal behavior. Future work will include developing a thermal conductivity relationship for specifically for the WIPP RoM salt so we can accurately model thermal behavior.

Experiments and Modeling in Support of Generic Salt Repository Science

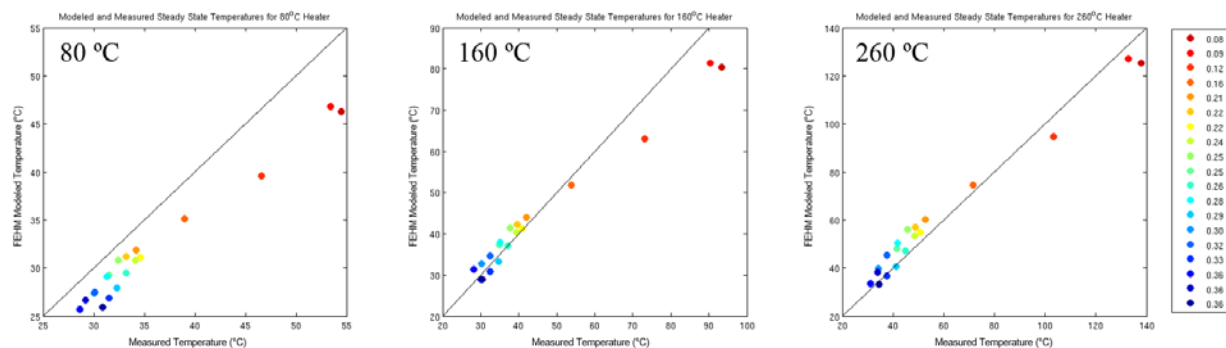


Figure 33: Simulated steady-state temperatures for all thermocouples compared to measured temperatures for three simulation (80, 160, and 260 °C), plotted against the 1:1 line. Note the warm colors are locations close to the heater, the farther locations are represented by cooler colors.

6.3.2 Water vapor behavior in RoM salt

In previous examinations performed in granular salt we found that the relative humidity (RH) in the air space above the salt stabilizes at between 30 and 35 % when the air space is vented, which is within few % points of the relative humidity in the air in the laboratory. However, when the box is insulated from the exterior the RH slowly increases until it reaches ~ 70 % (Figure 34). The ponded water at the bottom of the salt box provides a moisture supply that rises to the airspace and increases the relative humidity. It is worth noting that this rise in RH is very slow considering that the diffusion through the salt should be much faster. This is attributed to the strong hygroscopic properties of the salt that strongly absorb the water and delay their transport.

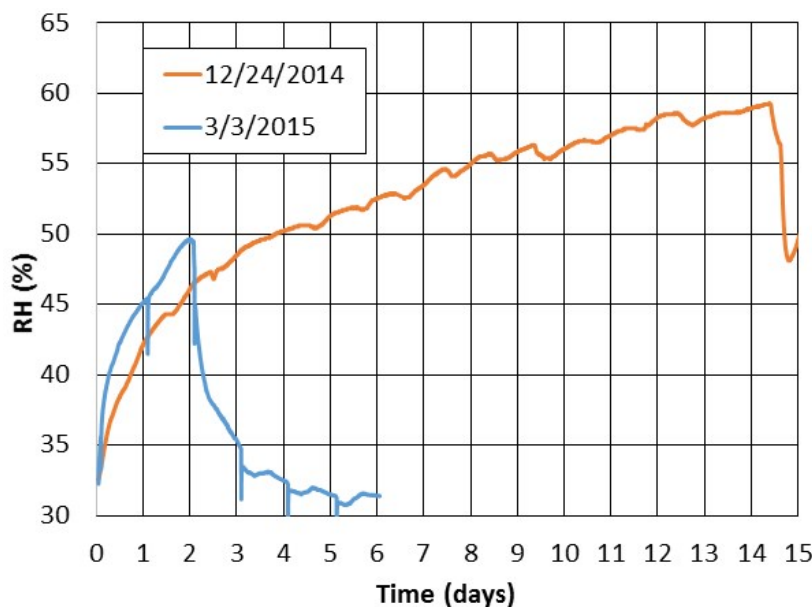


Figure 34: Relative humidity in the airspace above the salt in a box filled with granular salt with 2.0 wt.% brine ponded at the bottom of the salt box.

The behavior of the relative humidity in the air space above the salt is significantly different when the salt used is RoM salt from WIPP. The data in Figure 35 show RH in a sealed box at ambient temperature (up to days 30) and following powering the heating block to 80 °C.

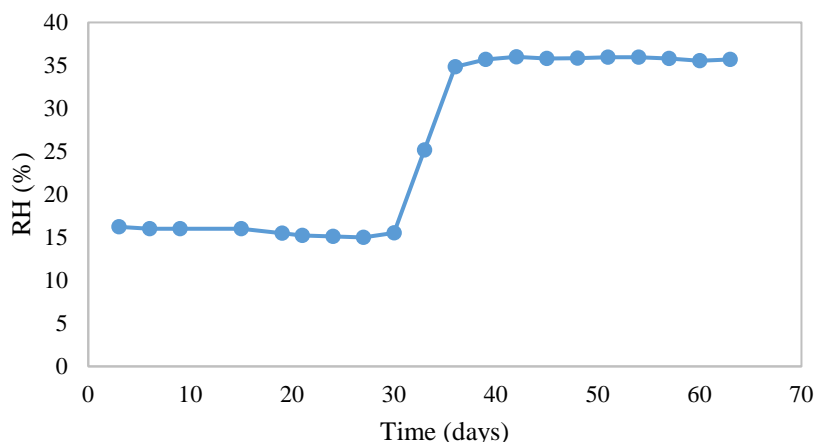


Figure 35: Relative humidity in the air space above the RoM salt under ambient conditions and when the heating block is powered to 80 °C.

Under ambient conditions the RH is very low and several % below the ambient RH of the air in the laboratory. This is attributed to the RoM salt and accessory minerals which desiccate the air in the salt box very rapidly. When the temperature is increased the RH increases to about ~35 % and remains stable. We attribute this to dehydration of the accessory minerals which supplies the additional moisture in the air raises the RH. When the block is heated to higher temperatures, the RH rises even higher. This is again attributed to the further dehydration of the accessory minerals as a hotter block will have a larger heat envelope, affecting a larger volume of salt, and therefore inducer more dehydration.

We examined the capacity of the RoM salt to buffer the relative humidity in the air inside the salt box by injecting a constant flow of air with a RH of 69 % at the bottom of the salt pile. The air flow was fixed to 0.67 L/min and the experiment ran for several months. The data in Figure 36 show the relative humidity in the air gap above the salt. The data show that the salt pile completely desiccates the air that flows through the salt and the RH rises very slowly. After 2 months of continued flow the relative humidity is still below the ambient RH of the air in the laboratory. There are no indications of water ponding in the box. It is clear that the accessory minerals associated with the salt are strongly influencing the water vapor flow through the salt.

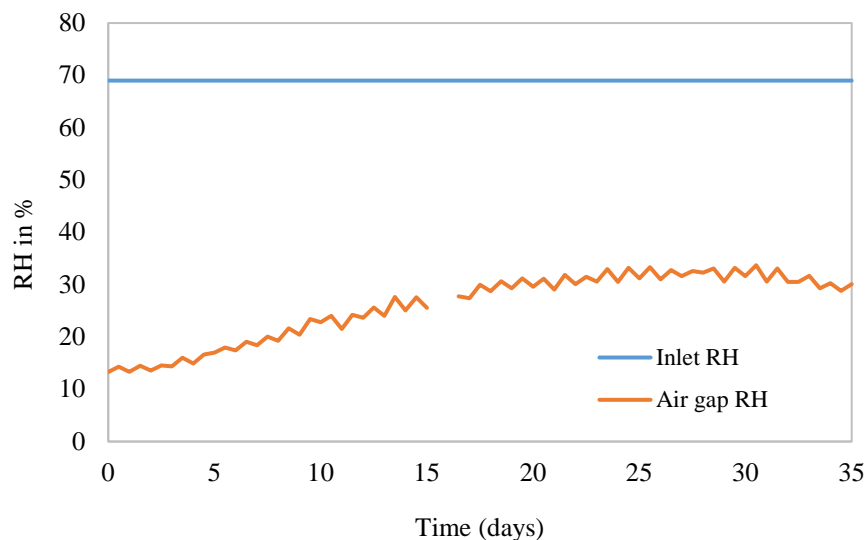


Figure 36: Relative humidity in the air gap above the salt and in the air flow circulated through salt. The experiment was performed at ambient temperature of 23.5 °C. The salt properties are summarized in Table 5.

6.3.3 Tracer breakthrough experimental data and modeling

A tracer test was performed under ambient temperature conditions to characterize the transport of tracers in the packed salt box before any significant changes occur as a results of heating (Figure 37). The salt properties are well defined and are summarized in Table 5. However, the porosity of the salt packed in the box, tortuosity and pore connectivity are unknown. We used our current parameterized FEHM model to fit the tracers break through data.

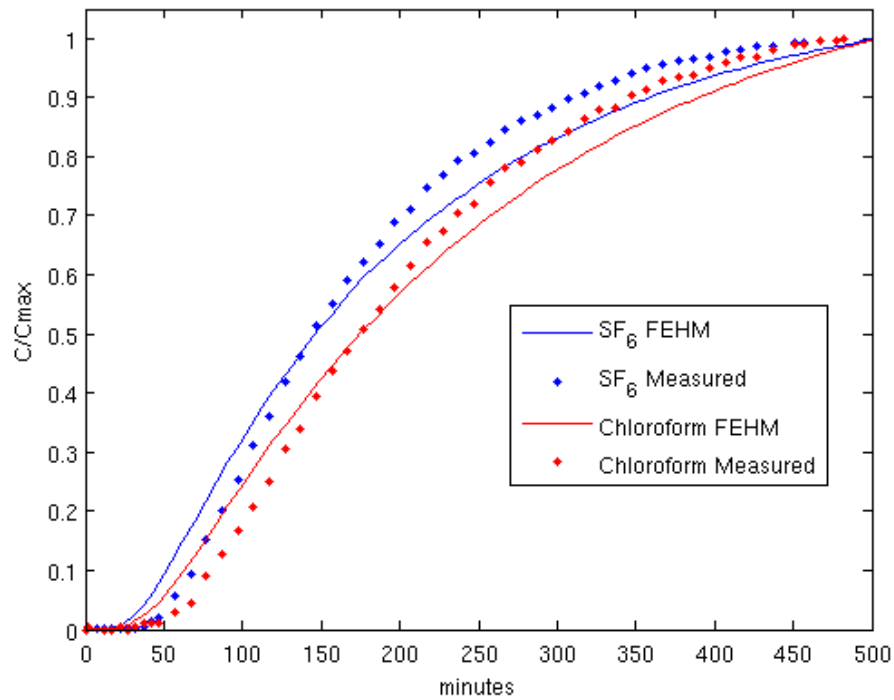


Figure 37: Breakthrough curves for tracer gases SF₆ (experimental data = squares, fit = solid line) and Chloroform (experimental data = diamonds, fit = dotted line) performed under ambient temperature conditions before heating. Tracer test T1.

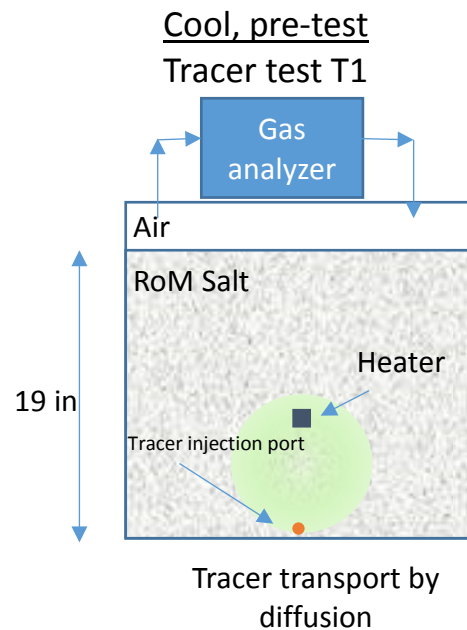


Figure 38: Schematic representation of the tracer test performed under ambient temperature conditions immediately after setting up the salt box. Conditions: Temperature = 23.5 °C, Air flow recirculation, Heater temperature = ambient, salt height = 19 inches, moisture content in salt 0.19 wt.%, RH in air gap = 15%.

The modeling was performed using the experimental setup described in Section 6.3.1. We have only completed preliminary modeling of this experiment, so the fit to the measured data needs adjustment. SF_6 arrives earlier and with greater concentration than chloroform because of its higher diffusivity and non-reactive behavior. The fit shown in Figure 37 is the result of a first attempt using reasonable guesses for the input parameters. The current input parameters are available in Table 5, and also use the free-air diffusion coefficients for SF_6 and chloroform of $9.68e^{-6} \frac{\text{m}^2}{\text{s}}$ and $8.66e^{-6} \frac{\text{m}^2}{\text{s}}$, respectively. Adjusting parameters, such as porosity and water content/saturation, will change the arrival time and relative concentrations of the gases. Fitting the breakthrough curves by optimizing for porosity and water content will help to determine these parameters for the heater experiments.

Tracer tests were also performed immediately after heating the salt box to various temperatures and up to two weeks after the temperatures were held at a steady state at the designated temperature. The data in Table 7 summarize the tracer studies performed. Breakthrough curve fitting of the ambient conditions, as well as tracer injections at higher temperatures, will be continued in future work.

Table 7: Summary of the tracer test performed in RoM salt.

Block heater temperature	Tracer test ID	Heater start date	Tracer test date	Tracer test date	Tracer test date
ambient	T1	-	1-19-2016		
80 °C	T2,T3	1-26-2016	1-26-2016	1-27-2016	02-10-2016
160 °C	T4,T5	02-17-2016	02-17-2016	03-02-2016	
260 °C	T6,T7	03-15-2016	03-15-2016	03-21-2016	

The tracer data for the initial tracer test initialed immediately after rising the temperature to 80 °C and two weeks later is shown in Figure 39.

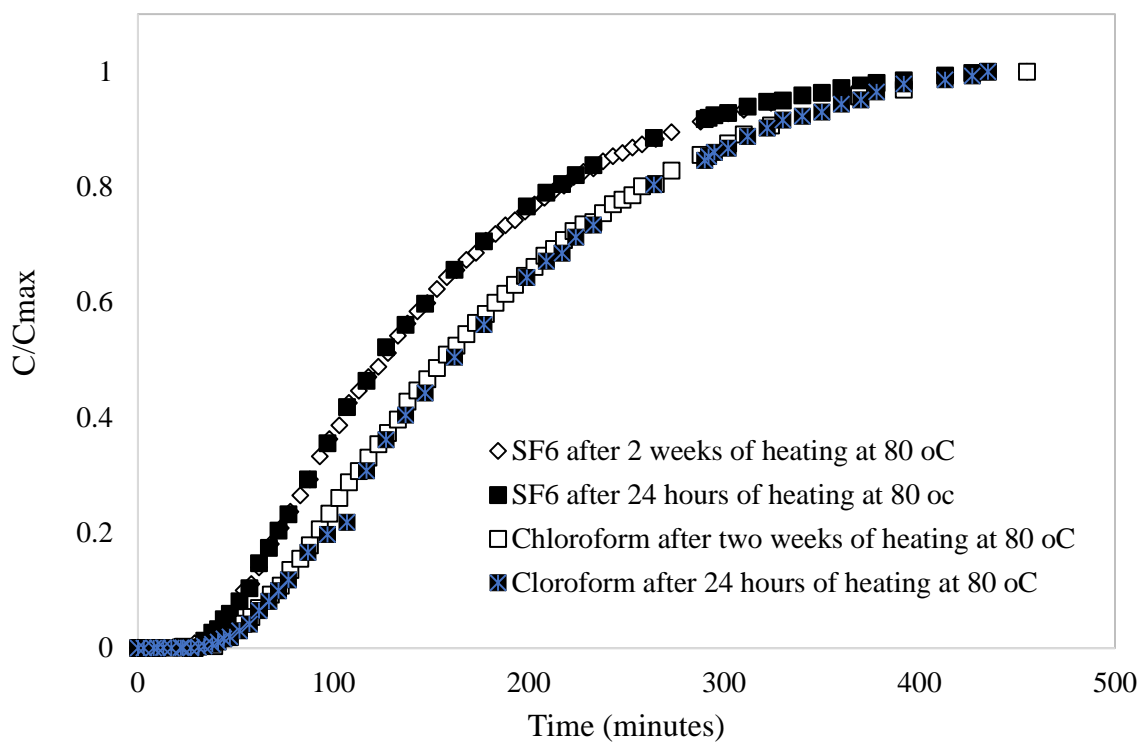


Figure 39: Breakthrough curves of tracer gases at ambient temperature and at 80 °C. Filled and empty diamonds show the breakthrough of SF6 at ambient conditions and following heating at 80 °C for 24 hours and after two weeks. Filled squares and stars filled squares show the breakthrough of Chloroform at ambient conditions and following heating at 80 °C for 24 hours. Tracer tests T2 and T3.

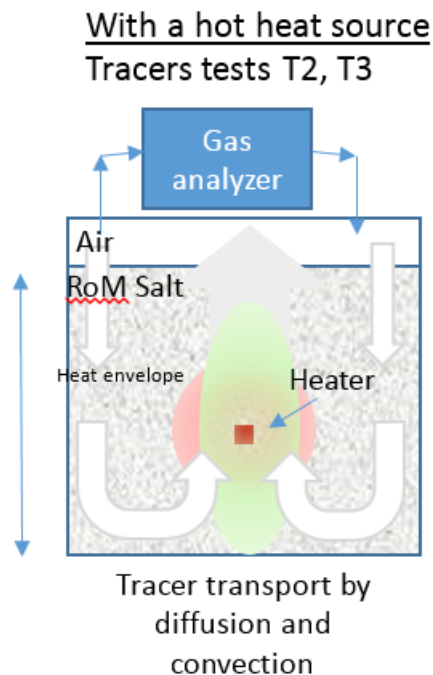


Figure 40: Schematic representation of tracer tests performed under heating conditions. The schematics show a convection process that pushes hot air to the air gap and recirculates cold air back to the bottom of the box. Temperature = 80 °C, Air flow recirculation, Heater temperature = ambient, salt height = 19 inches, moisture content in salt 0.19 wt.%, RH in air gap = 35%.

The breakthrough data show that there are no measurable differences in the breakthrough curves of the tracer gases at 24 hours and after 14 days of constant heating. This indicates that there are no noticeable changes in the structure of the salt following heating. However, the tracers breakthrough are markedly different from the ambient conditions, which is expected because gas diffusivity increases with temperature. There is also a convection process in the salt box that causes hot air from around the heater to rise to the air gap and for cooler air from the air gap to recirculate down the bottom of the box (Figure 40). This convection process enhances the rate of the gas breakthrough. The data also show that at 80 °C SF_6 transports faster than chloroform. This is again attributed to the moisture present in the salt, which will delay chloroform transport because of its partitioning in the water. There might be some artifact from the box enclosure walls which also have an affinity to chloroform and will also contribute to its retardation.

The data summarizing tracer tests T4-T7 performed at 160 °C and 260 °C are summarized in Figure 41.

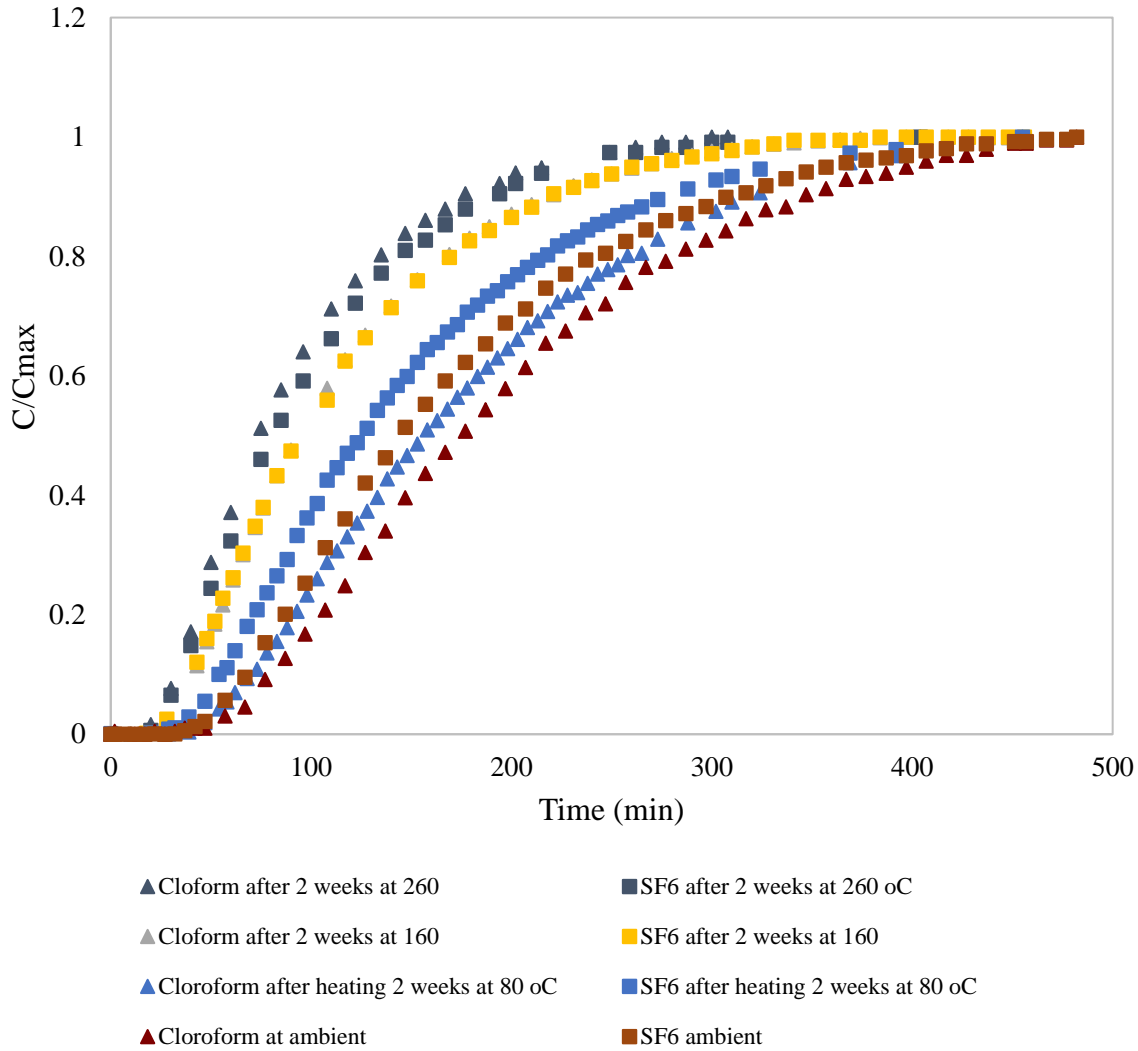


Figure 41: Tracer breakthrough results showing data for SF₆ and Chloroform at different temperatures. Triangles represent Chloroform breakthrough and squares represent data for SF₆. The different temperatures are indicated in the figure caption.

The data show a consistent shift of the breakthrough curves indicating fast transport of the tracers as the temperature rises. We did not observe any changes in the breakthrough curves with time when the temperature was maintained constant. Even at 260 °C, breakthrough curves at 24 hours were identical to the breakthrough curves after one week of constant heating. Chloroform breakthrough at the hottest temperature becomes almost identical to SF₆ and loses any retardation effects that are caused by the salt and the enclosure walls.

6.3.4 *Post heating forensics examination of salt dissolution and re-precipitation*

Porosity changes in heated granular salt

When the experiment was concluded, the salt bed was excavated to obtain samples and determine porosity. Samples of salt were taken from the top down, starting at 21 inches from the bottom of the box (table 1). Once a sample was obtained, it was vacuum impregnated with indigo blue colored epoxy, and then prepared into a thin section. The section was photographed, area of interest bounded, and then total and blue pixels determined. Porosity was calculated as blue/total pixels. These porosity values are reported in Table 8.

Table 8: Porosity data of forensic samples. Depth and porosity information from excavated samples.

Depth in inches	Sample number	Porosity
21" from base	30	47.26
13"	31	54.61
11"	32	52.44
9"	33	50.77
7"	34	52.35
5"	35	49.21
3" (direct above saturation line	36	51.21
top of heater	37	42.04
box corner above saturation line	38	43.32
adjacent to heater	39	23.58

Thin Section characterization

The thin sections analysis revealed quantification issues immediately. Samples where most of the crystals “bridge” to each other due to recrystallization can be considered intact and valuable for porosity calculation. This is very important since heat treated salt samples may be extremely friable and capable of falling apart. Such is the case when dissolution occurs but recrystallization is not immediate and local. Therefore, certain samples listed in Table 8 may not accurately represent true porosity.

A good example of sample dis-aggregation can be viewed in Figure 39. This sample (S-31) shows rounding of grain corners, which is indicative of dissolution of the salt grains. However, there is little evidence of grains bridging to each other via recrystallization. In fact, the sample is dominated by crystals floating in the blue epoxy matrix. This sample would not give a true porosity value. This is also true of sample S-34 (Figure 44). The rest of the samples range from minimal recrystallization (Figure 44 “S-33” and “S-34”) to abundant recrystallization and “bridging” of grains (samples in Figure 46 “S-38 and S-39”).

Although the porosity values of Table 8 are not strictly quantitative, those values along with careful petrographic interpretation is a strong indicator of dissolution and re-precipitation

events caused by water/vapor transport in the granular salt experiment. All samples except the sample near the heater experienced significant dissolution and variable re-precipitation. Those at a distance from the heater element (Samples S-31 and S-32 in Figure 43) exhibit moderate dissolution and minimal re-precipitation. As one approaches the heater, porosity drops slightly indicating both dissolution and re-precipitation. Those samples with lower porosity (samples S-37 and S-38, Figure 46) of approximately 42% may have had significant dissolution and re-precipitation occurring due to heat and water proximity. Sample S-39 (23.6 % porosity) may have been subject to boiling and precipitation events, resulting in reduced porosity from the original 35 %.



Figure 42: Sample S-30



Figure 43: Sample S-31

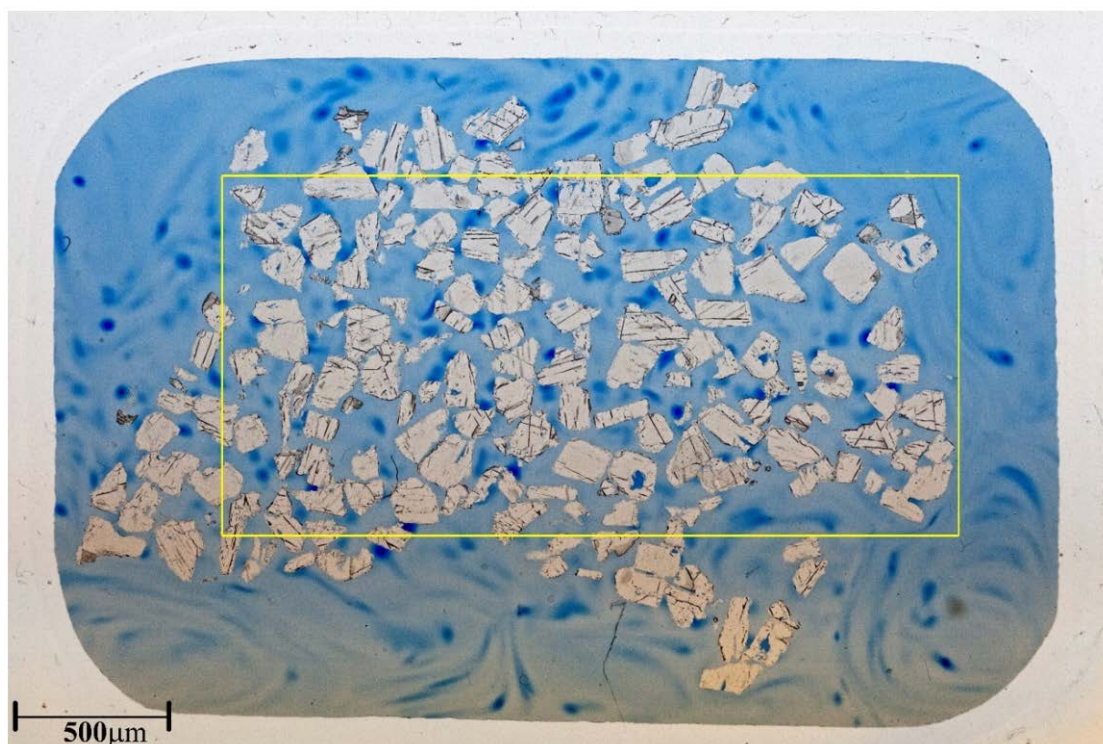


Figure 44: Sample S-34

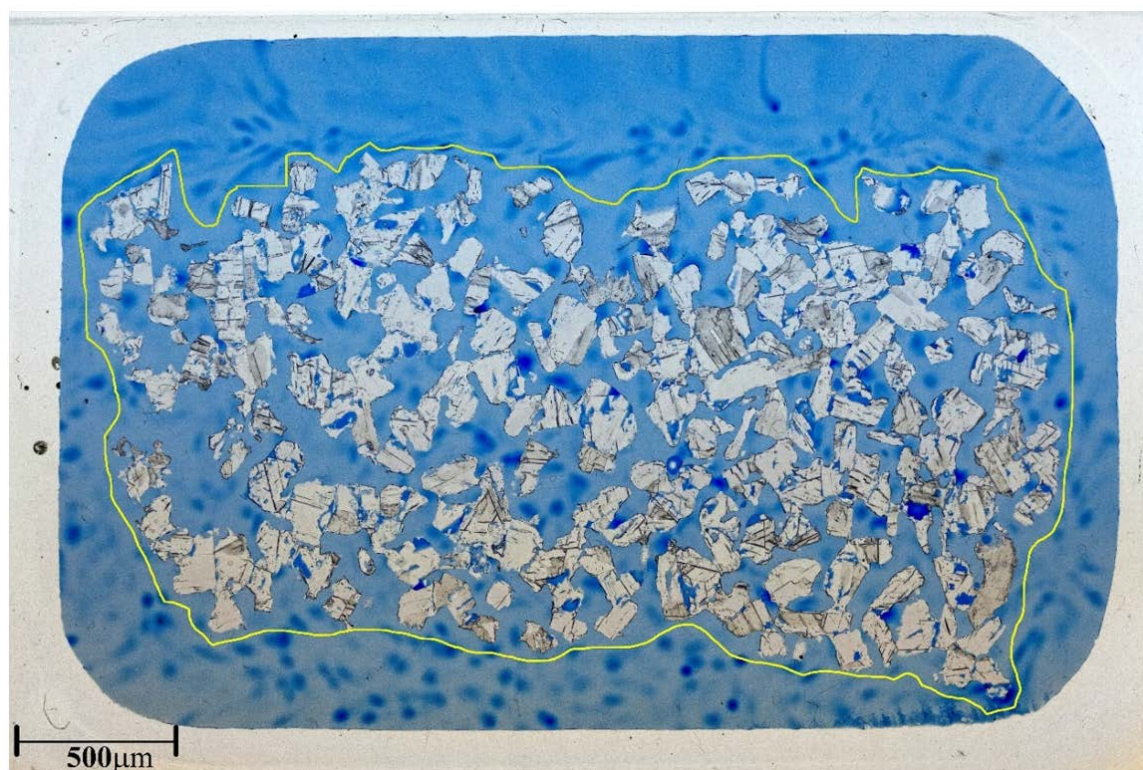


Figure 45: Sample S-36



Figure 46: Sample S-38

7 Reanalysis of drift scale salt canister simulations

7.1 Objectives

Previous modeling work described in (Stauffer 2015) was undertaken to characterize a metal canister encased in salt. That work was done prior to the release of the FEHM salt module, and necessitated amendments directly to the FEHM source code. “Hacking” code in this manner is inefficient because relatively few users can properly manage it, and errors introduced during the code amendment process can cause problems for model runs. This factor was the motivation for the development of the salt module with user specified conditions. Following the development of the salt module and subsequent code amendments in the August 1, 2016 FEHM version, this canister setup was rerun in order to compare the salt module and “hacked” versions in terms of run time, timestep size and quantity, and model iterations necessary to achieve convergence. It would be expected that the salt module would have performance at least as good as the earlier model run.

7.2 Model setup

The model domain is shown in Figure 47. It is a quarter-space simulation of a salt gallery repository. Several metal canisters are buried in a trapezoidal prism of crushed salt. The crushed salt is surrounded by air with a capstone ceiling above and floor below of intact salt. For future simulations of humidity, gas flux can be applied in the air zones with specified humidity. Salt properties for intact salt are as described above in Table 3. Crushed salt surrounding the canisters has slightly different properties (Table 9).

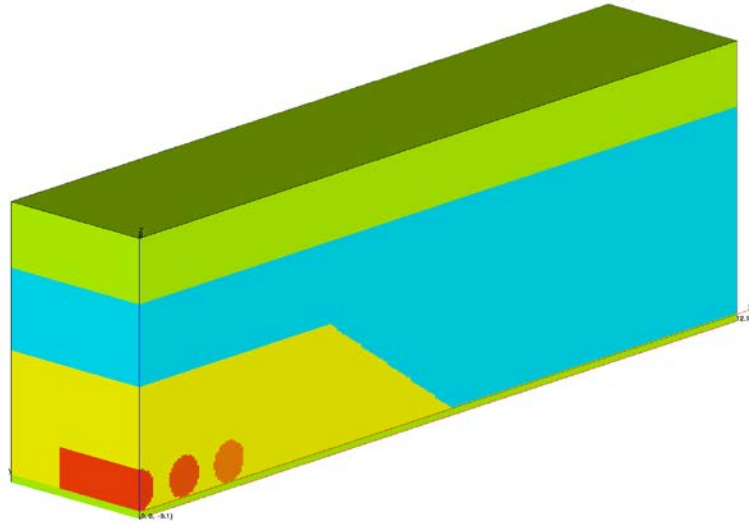


Figure 47: Salt canister model domain. Canisters are shown in orange, damaged salt in yellow, air in blue, and intact salt in green.

Table 9: Parameters of difference between intact and damaged salt for canister runs.

Parameter	Damaged salt value	Intact salt value
Porosity	0.35	0.001
Permeability	10^{-12} m^2	$10\text{-}20 \text{ m}^2$

7.3 Results

If the salt module has easier solution convergence, the timesteps should be slightly larger and the salt module should gradually advance ahead of the old version, eventually resulting in fewer timesteps. In this regard, the salt module was successful; the old model required 7705 timesteps to complete 830 days, while the new version took 7239 timesteps. As a result, each individual timestep in the new version was slightly larger (Figure 48a). Numerical results are comparable between the two runs except for values which are sensitive to timestep sizes, such as fluxes. In these cases, rates are still similar.

Runtimes for the first 100 timesteps were comparable between the two models (Figure 48b). Then for a brief period the old model ran faster, but the new version achieved temporal parity by 2000 timesteps. By the final timestep, the salt module had completed in 84,460 fewer seconds. Caution should be exercised when comparing model times because other factors such as

processor demands can influence the time to run models. Nevertheless, a full day's improvement in runtime is large enough to suggest that the salt module provides a significant improvement in runtimes for large model runs.

The comparison of Newton-Raphson (NR) iterations (Figure 48c) shows similar tendencies to model run time, with the difference in efficiency increasing over longer model runs. By the final timestep, the total number of NR iterations in the salt module was down to 42% of the total required by the early version. Likewise, the total solver runs (Figure 48d) was very different between the two versions, with a full order of magnitude decrease in the number of iterations required by the new version. The differences in NR and solver iterations probably accounts in large part of the improved performance time of the salt module.

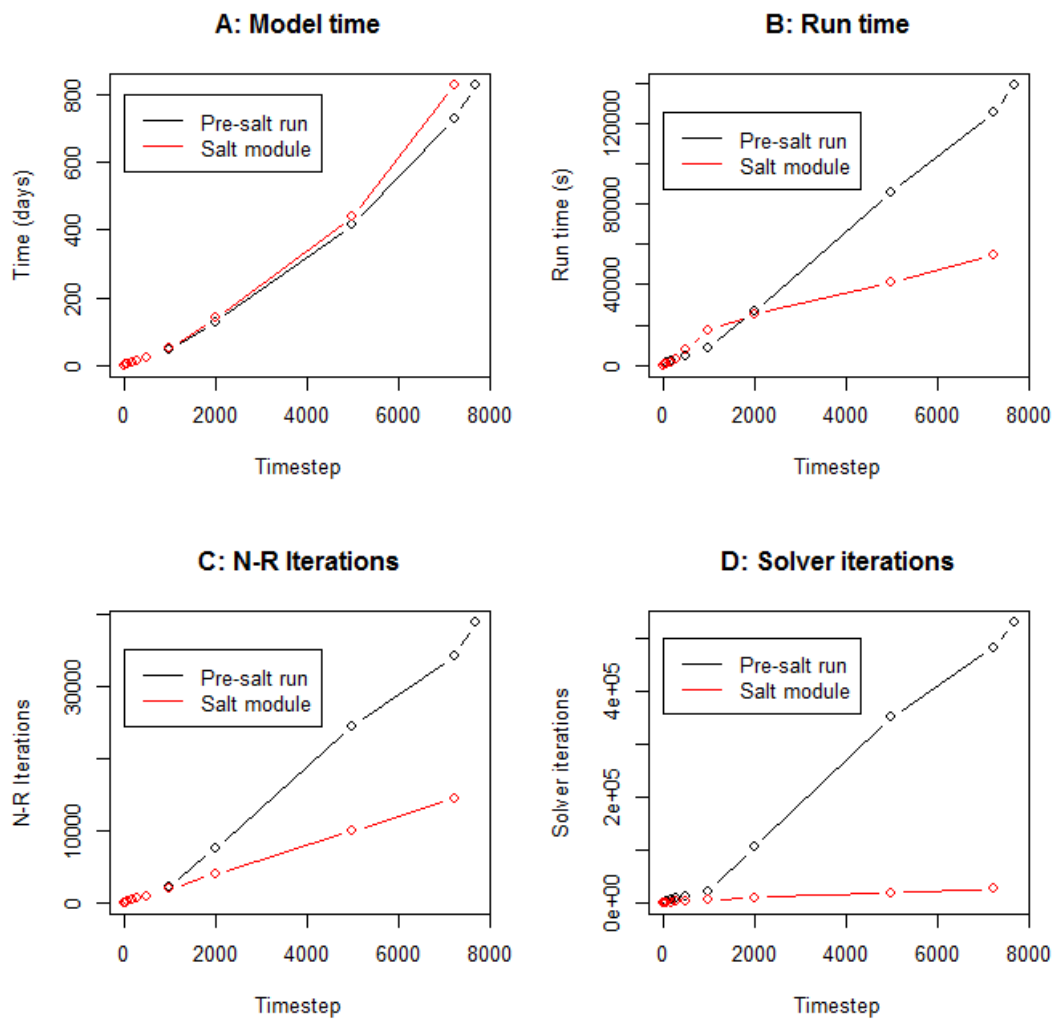


Figure 48: Comparison of “hacked” FEHM code model run performance vs. the August 2016 model version. The rate of model time advancement (a), the CPU time necessary for the model to run (b), Newton-Raphson iterations (c), and total Solver iterations (d) are compared.

8 Future Work

Several focus areas are planned in order to ensure that numerical modeling using FEHM can accurately provide insight for the investigation of application-scale problems at WIPP and elsewhere. The work plan for FY2017 will include laboratory experiments and FEHM code changes and developments to support a test plan for underground field test design of an in-situ small diameter borehole thermal test. Prerequisite laboratory test and preliminary modeling will be performed to isolate specific processes and behaviors, in a controlled environment, and make initial predictions prior to the test.

A priority for code development is to add in a dynamic water retention curve for the *rlp* control statement, which determines the relative permeability of water and gas depending on porosity and capillarity. Brine and gas migration may be complicated by capillarity that changes with thermal conditions due to dissolution and precipitation. Several capillary models are possible for salt (Cinar et al., 2006). User-specified tabular models have been applied to the modeling work investigating the Olivella et al. (2011) experiments, in which capillary pressure is a function of saturation. However, capillarity is a function of both saturation and porosity, but modeling work described by the Olivella et al. (2011), as well as the present FEHM simulations, both use capillary retention curves for a single porosity value. Code additions to allow for determination of capillarity based on changes in saturation and porosity are presently being undertaken to allow for improved specification of a representative relative permeability model that can change during simulation time.

Additionally we plan to continue work for determining specific thermal properties of WIPP salt. Parameter optimization is planned to develop thermal conductivity relationships for WIPP by using the experiments describe in Section 6. Curve fitting to the tracer gases released during the experiments will also allow for informing temperature-dependent gas diffusivity. Since the predicted and observed changes to porosity and permeability are primarily due to the migration of variable-temperature air and water vapor, properly constraining this value is important in order to correctly model the gas migration.

Comparison to simple bench experiments that support the underground test plan highlight the needed code modification for FEHM; the bench-scale experiments drive the code development in the effort to support the underground test plan being developed in 2017.

References

- Bechthold, W., E. Smailos, S. Heusermann, W. Bollingerfehr, B. Sabet, T. Rothfuchs, P. Kamlot, J. Grupa, S. Olivella, and F.D. Hansen. 2004. Backfilling and sealing of underground repositories for radioactive waste in salt (Bambus II project). Final Report for European Atomic Energy Community EUR 20621, Office for Official Publications of the European Communities, Luxembourg. Birkholzer, J.T. 2004. Estimating liquid fluxes in thermally perturbed fractured rock using measured temperature profiles. *J. Hydrol.* 327 (3-4): 496-515, doi 10.1016/j.jhydrol.2005.11.049.
- Bodvarsson, G.S., W. Boyle, R. Patterson, and D. Williams. 1999. Overview of scientific investigations at Yucca Mountain—the potential repository for high-level nuclear waste. *J. Contam. Hydrol.* 38 (1): 3–24, doi 10.1016/S0169-7722(99)00009-1.
- Caporuscio, F.A., H. Boukhalfa, M.C. Cheshire, A.B. Jordan, and M. Ding. 2013. Brine Migration Experimental Studies for Salt Repositories, FCRD Used Fuel Disposition Campaign Milestone FCRD-UFD-2013-000204, September 25, 2013.
- Cinar, Y., G. Pusch, and V. Reitenbach. 2006. Petrophysical and capillary properties of compacted salt. *Transp. Porous Media* 64 (2): 199-228.
- Domalski, E.S., and E.D. Hearing. Condensed Phase Heat Capacity Data. In: P.J. Linstrom and W.G. Mallard, editors, NIST Chemistry WebBook, NIST Standard Reference Database Number 69. National Institute of Standards and Technology, Gaithersburg, MD. <http://webbook.nist.gov> (accessed June-July 2016).
- Doughty, C., and K. Pruess. 1990. A similarity solution for two-phase fluid and heat flow near high-level nuclear waste packages emplaced in porous media. *Int. J. Heat Mass Transfer* 33(6): 1205–1222.
- Hansen, F.D., and C.D. Leigh. 2011. Salt disposal of heat-generating nuclear waste. Sandia National Laboratories Report SAND2011-0161. Albuquerque, NM.
- Jordan, A.B., H. Boukhalfa, F.A. Caporuscio, and P.H. Stauffer. 2015a. Brine Transport Experiments in Run-of-Mine Salt. Los Alamos National Laboratory Report LA-UR-15-26804. Los Alamos, NM.
- Jordan, A.B., Zyvoloski, G.A., Weaver, D.J., Otto, S., and Stauffer, P.H., 2015b. Coupled Thermal-Hydrologic-Chemical Model for In-Drift Disposal Test. Los Alamos National Laboratory Report LA-UR-15-27442. Los Alamos, NM.
- Jordan, A.B., H. Boukhalfa, F.A. Caporuscio; B.A. Robinson, P.H. Stauffer. 2015c. Hydrous Mineral Dehydration around Heat-Generating Nuclear Waste in Bedded Salt Formations, *Environmental Science & Technology*, 5:1-13. DOI: 10.1021/acs.est.5b01002.
- Kelly, W.R. 1985. Brine migration in salt: Topical report. <http://pbadupws.nrc.gov/docs/ML0404/ML040410467.pdf> (accessed 10 July 2013).
- Kelkar, S., G. WoldeGabriel, and K. Rehfeldt. 2011. Hot Dry Rock Geothermal Energy Development at Los Alamos National Laboratory: 1970-1995, Final Report. Los Alamos National Laboratory Report LA-14433-HDR.

- Krieg, R.D. 1984. Reference Stratigraphy and Rock Properties for the Waste Isolation Pilot Plant (WIPP) Project. Sandia National Laboratories Report, SAND-83-1908.
- Kuhlman, K.L., and B. Malama. 2013. Brine Flow in Heated Geologic Salt. Sandia National Laboratories Report SAND2013-1944. Albuquerque, NM.
- Lappin, A.R. 1988. Summary of site-characterization studies conducted from 1983 through 1987 at the Waste Isolation Pilot Plant (WIPP) site, southeastern New Mexico. In: Post, R.G.; High-level waste and general interest: Volume II, p. 371-376. Waste Management: Symposium on Radioactive Waste Management, Tucson, AZ, 28 Feb – 3 Mar 1988.
- Olivella, S., S. Castagna, E.E. Alonso, and A. Lloret. 2011. Porosity variations in saline media induced by temperature gradients: experimental evidences and modeling. *Transport in porous media*, 90(3): 763-777.
- Pollock, D.W. 1986. Simulation of Fluid Flow and Energy Transport Processes Associated With High-Level Radioactive Waste Disposal in Unsaturated Alluvium. *Water Resources Research*, 22(5): 765-775.
- Robinson, B.A., N.Z. Elkins, and J.T. Carter. 2012. Development of a US Nuclear Waste Repository Research Program in Salt. *Nuclear Technology*, 180(1): 122-138.
- Rutqvist, J. L.B. Martin, S. Molins, D. Trebotich, and J. Birkholzer. 2016. Modeling Coupled THM Processes and Brine Migration in Salt at High Temperatures, UFD Document FCRD-UFD-2015-000366, LBNL-191216.
- Rutqvist, J., D. Barr, R. Datta, A. Gens, A. Millard, S. Olivella, C.-F. Tsang, and Y. Tsang. 2005. Coupled thermal–hydrological–mechanical analyses of the Yucca Mountain Drift Scale Test—Comparison of field measurements to predictions of four different numerical models. *International Journal of Rock Mechanics and Mining Sciences*, 42(5): 680-697.
- Stauffer, P.H., D.R. Harp, A.B. Jordan, Z. Lu, S. Kelkar, Q. Kang, J. Ten Cate, H. Boukhalfa, Y. Labayed, P.W. Reimus, F.A. Caporuscio, T.A. Miller, and B.A. Robinson. 2013. Coupled model for heat and water transport in a high level waste repository in salt; Los Alamos National Laboratory Document, LA-UR-13-27584.
http://www.energy.gov/sites/prod/files/2013/12/f5/CouplModelHeatWaterTransprtGenericH LWRepSalt_1.pdf.
- Stauffer, P.H., A.B. Jordan, D.J. Weaver, F.A. Caporuscio, J.A. Ten Cate, H. Boukhalfa, B.A. Robinson, D.C. Sassani, K.L. Kuhlman, E.L. Hardin, S.D. Sevougian, R.J. MacKinnon, Y. Wu, T.A. Daley, B.M. Freifeld, P.J. Cook, J. Rutqvist, and J.T. Birkholzer. 2015. Test proposal document for phased field thermal testing in salt; FCRD Used Fuel Disposition Campaign Milestone FCRD-UFD-2015-000077, April 30, 2015.
- Zyvoloski, G.A. 2007. FEHM: A control volume finite element code for simulating subsurface multi-phase multi-fluid heat and mass transfer. Los Alamos National Laboratory Report LA-UR-07-3359. Los Alamos, NM.
- Zyvoloski, G.A., B.A. Robinson, Z.V. Dash, and L.L. Trease. 1997. Summary of the models and methods for the FEHM application—A finite element mass-and heat-transfer code. Los Alamos National Laboratory Report LA-13307-MS, modified 1999. Los Alamos, NM.

Appendix A: Additions and Usage of New Humidity Boundary Conditions

Humidity-Related Boundary Conditions, Source/Sink Terms and Initial Conditions

George Zyvoloski July 24, 2016

This summary organizes in one place the humidity-related input in FEHM. Grid blocks can have inflow of liquid water and/or air. These flows can be induced by constant pressure conditions, constant saturation conditions, or specified flow rate conditions. The new humidity boundary conditions can adjust these inflow streams to reflect fractions of air and water that in turn represent humidity at prescribed temperature, and pressure conditions. It should be noted that with specified pressure, the flow can be inflow or outflow. Attributes for the flow like temperature, air mass fraction, and humidity can only be specified for inflow. If the flow at a specified pressure turns is outflow then temperature and mass fractions cannot be specified and “in place” values are used in the conservation equations. Humidity in this document refers to the relative humidity fraction: $\text{humidity} = P_{v_{h2o}}/P_{vsat_{h2o}}(T)$.

General algorithmic and output improvements

Over the past fiscal year, improvements related to humidity were made in FEHM in the following areas:

1. Very low water vapor pressure. FEHM was modified to handle vapor pressures as low as 1.e-9 Mpa. This allowed complete dry out to occur smoothly improved the nonlinear iteration of the fluid and energy balance equations
2. Outflow boundary conditions. Allow constant pressure boundary conditions to induce gas discharge (with water vapor) in grid blocks with no liquid water (phase state 3) or to extract liquid water via saturation and humidified gas via constant pressure (phase state 2)..
3. Humidity initialization. Allows the setting of humidity at initial temperature and pressure conditions. (Form is similar to setting the water partial pressure at a specified temperature.)
4. The humidity fraction is calculated and given in the output file. The humidity fraction is already available as output for contour plots. This is a portion of the new output file:

Nodal Information (Gas)

	Partial P	Capillary	Liquid	Gas source/sink			
Node	Gas (MPa)	Pres (MPa)	Pres (MPa)	(kg/s)	Residual	State	R humidity (fraction)
1	0.9902E-01	0.000	0.1000	0.000	0.000	2	1.000
10	0.9902E-01	0.000	0.1000	0.000	0.000	2	1.000
101	0.9902E-01	0.000	0.1000	0.000	0.000	2	1.000
321	0.9901E-01	0.000	0.1000	0.000	0.000	2	1.000
621	0.9900E-01	0.000	0.1000	0.000	0.000	2	1.000
622	0.9855E-01	0.000	0.1000	-0.1818E-08	0.000	3	.4615
93	0.9901E-01	0.000	0.1000	0.000	0.000	2	1.000

Experiments and Modeling in Support of Generic Salt Repository Science

122	0.9901E-01	0.000	0.1000	0.000	0.000	2	1.000
123	0.9866E-01	0.000	0.1000	0.1058E-07	0.000	3	.4261
275	0.9842E-01	0.000	0.1000	0.000	0.000	3	.5000

Control statement ngas (optional)

Non condensable gas transport. Note that Group 3 and Group 4 have 1 additional input variable

Group 1 - ICO2D

Group 2 - JA, JB, JC, PNGAS (JA, JB, JC - defined on page 33)

Group 3 - JA, JB, JC, HUMN, PFLOWN (JA, JB, JC - defined on page 33)

Group 4 - JA, JB, JC, QCD, AIPEDN (JA, JB, JC - defined on page 33)

Note that all Group 2 values are entered first, followed by Group 3 values, followed by Group 4 values. Note that all Group 2 values are entered first, followed by Group 3 values, followed by Group 4 values.

ICO2D - integer (3) - Solution descriptor for non condensable gas transport.

ICO2D = 1, the 3 degree of freedom solution will be reduced to a 1 degree of freedom problem. (See macro **iter**, the parameter ICOUPL is also set to 5 if ICO2D = 1.)

ICO2D = 2, the 3 degree of freedom solution will be reduced to a 2 degree of freedom problem. (See macro **iter**, the parameter ICOUPL is also set to 5 if ICO2D = 2.)

ICO2D = 3, full 3 degree of freedom.

PNGAS - real (0), Initial partial pressure of noncondensable gas. If PNGAS < -1 then ABS (PNGAS) is interpreted as a temperature and the partial pressure of the noncondensable gas is calculated according to the formula: $PNGAS = PT - PSAT(T)$ where PT is the total pressure and $PSAT(T)$ is the water saturation pressure and is a function of temperature only. If $-1 < PNGAS < 0$ then ABS (PNGAS) is interpreted as the relative humidity fraction (H) and the partial pressure of the noncondensable gas is calculated according to the formula: $PNGAS = PT - H * PSAT(T)$. Here T is the initial temperature that is inputted in the pres macro or in a restart file.

HUMN - real (0). If HUMN < or = 0, then ABS (HUMN) is the specified saturation and will add or remove water to maintain that value.

If HUMN >, then HUMN is the specified relative humidity and the saturation, *Sl*, is calculated using the vapor pressure lowering formula and the capillary pressure formula:

$$P_{cap}(Sl) = \ln(HUMN) * den * RT$$

where *Pcap* is the capillary function, HUMN is the humidity, *R* is the gas constant, *T* is the temperature, and *den* is the liquid density. Once the formula is solved, *Sl* is held constant.

The humidity condition is only enabled for the van Genuchten capillary function model. See macro **rlp**.

NOTE: 0.0 is a valid entry for HUMN. To turn off the humidity/saturation. enter -888.

PFLOWN- real (0). Specified ngas partial pressure (Mpa). Noncondensable gas will be added or removed to maintain the specified value.

QCD - real (0). Specified air source strength (kg/sec).

AIPEDN - real (0). Impedance factor(kg/sec-Mpa). If AIPEDN is non zero, QCD is interpreted as a fixed mass fraction of the inflow of the noncondensable gas with AIPEDN being the impedance factor (see macro **flow**). Must be associated with the macro **flow** and a specified total pressure:

$$Q_{ngas} = AIPEDN * QCD * (P_{FLOW} - P)$$

$$Q_w = AIPEDN * (1. - QCD) * (P_{FLOW} - P)$$

Example 1:

ngas

3

1 0 0 -20. # 1

11 33 11 -0.1 0.09 # 2

1 23 11 -1.e-4 0.0 # 3

flow

11 33 11 0.1 -20. 1.e2 # 4

1 23 11 -1.e-8 -20. 0.0 # 5

EX 1:

ngas: 1. The initial air partial pressure is set to $P_{tot} - P_{sat}(T=20\text{ C})$. 2. The saturation is fixed at abs(-0.1) ,outflow only; gas outflow pres is set to 0.09 Mpa. 3. Air inflow is set to -1.e-4 kg/s.

flow: 4. Pressure is fixed at 0.1 Mpa. Flowing temperature is set to 20 C. 5. Water inflow set to -1.e-8 kg/s, flowing temperature set to 20 C.

Example 2:

```

pres
1 0 0 0.1 25 1.

ngas
3
1 0 0 -0.3. # 1.

11 33 11 0.1 0.09 # 2

1 23 11 0.999 1. # 3

flow
11 33 11 0.1 -20. 1.e2 # 4
1 23 11 0.2 -20. 1 # 5

```

```

#*****

```

Example 3:

```

ngas
3
1 0 0 -20. # 1

11 33 11 -888. 0.09 # 2

1 23 11 0.999 1. # 3

flow
11 33 11 -1.e-8 -20. # 4
1 23 11 0.2 -20. 1 # 5

```

```

#*****

```

EX 2:

ngas: 1. The initial air partial pressure is set to $P_{\text{tot}} - 0.3 \cdot P_{\text{sat}}(T=25 \text{ C})$. Note T set to 25 in pres macro. 2. The humidity fraction is fixed at 0.1 via VG capillary function ,outflow only; gas outflow pres is set to 0.09 Mpa. 3. Air inflow mass fraction is set to 0.999; applies to flow generated in macro flow at same nodes.

flow: 4. Pressure is fixed at 0.1 Mpa. Flowing temperature is set to 20 C. 5. Pressure set to 0.2 Mpa, flowing temperature set to 20 C.

EX 3:

ngas: 1. The initial air partial pressure is set to $P_{\text{tot}} - P_{\text{sat}}(T=20 \text{ C})$. 2. Outflow from fixed saturation or humidity is turned off (-888); gas outflow pres is set to 0.09 Mpa. 3. Air inflow mass fraction is set to 0.999; applies to flow generated in macro flow at same nodes.

flow: 4. Water inflow is set to $-1.e-8 \text{ kg/s}$. Flowing temperature is set to 20 C. 5. Pressure set to 0.2 Mpa, flowing temperature set to 20 C.

Using the boun macro

The discussion and examples presented above demonstrate how humidity conditions can be made with the ngas macro and utilizing flow rates that were setup in the flow macro. These conditions and a few more options are available with the boun macro. These include:

1. Specified water flow. This can be accomplished in the boun marco with the sw or dsw keywords. When the water *inflow* is generated this way, the total inflow stream (kg/s) can be divided into mass flowrate fractions of air (dry) and water using the fxa keyword. The mass fractions are specified directly when the fxa keyword. The flow can be divided this only in it is inflow.

2. Specified air flow. This can be accomplished in the boun marco with the sa or dsa keywords. When the air *inflow* is generated this way, the total inflow stream (kg/s) can be divided into mass flowrate fractions of air (dry) and water that represent air at a specified humidity using the huf keyword. The flow can be divided this only in it is inflow.
3. Specified total pressure (pw) or specified air pressure (pa). These keywords generate flow rates of water and air respectively. If the generated flow is an inflow. Then the keywords for water flow (fxa) or air flow (huf) can be applied. Even is the humidity conditions are applied and the flow is outflow, the in place conditions will dictate the flow composition.
4. Specified humidity. The keywords 'hu' and 'huf' designate the fixed humidity and the flowing humidity respectively. The 'huf' is used when a specified air flow is introduced elsewhere, the 'hu' key word is stand alone in that the sources of water and air are generated to force the humidity condition. The humidity condition is defined by a specified humidity, a specified pressure and a specified temperature. The keywords ph (humidity pressure) and th (humidity temperature) can be used with hu and huf.

Control statement boun (optional)

This input example shows how to use the boun macro to provide an incoming variable air flowrate (boun macro,sa)with a variable relative humidity (boun macro,huf).

To calculate mass fractions from relative humidity, density of air and water vapor are required. Hence pressure(boun macro,ph) and temperature(boun macro,th) are needed to densities. If either Ph or Th are not provided, standard condition(s) are assumed: 0.1 Mpa for P and 20 C for T. The outlet condition is a constant pressure.

Note that the variable humidified air inflow is only available with the boun macro:

Example 1:

```
boun
modell
ti_linear
2 0 1e20
sa
-1.e-8 -1.e-8
ph
0.1 0.1
th
30. 30.
t
30. 30.
huf
0.2 0.2
```

In model 1 'huf' fixes the humidity of the gas inflow at the time sequence shown to 0.2 and 0.2 . The humidity calculations are made at ph = 0.1 Mpa and th = 30 C. Note that the air temperature is held at 30 C as well, keyword 't'.The gas flow rate is given under 'sa' (-1.e-8 -1.e-8). Model 1 is applied to zone 1. Model 2 is a constant temperature condition (15 C). This model is applied to zone 3. Model 3 is a constant air pressure condition and flowing temperature. This model is applied to zone 4. Note the ngas macro sets the humidity in two zones at 0.2 and the temperature to 15 C in another zone.

Experiments and Modeling in Support of Generic Salt Repository Science

model 2

ti_linear

2 0 1e20

t

15. 15.

model 3

ti_linear

2 0 1e20

pa

0.1 0.1

ft

30. 30.

-1 0 0 1

-3 0 0 2

-4 0 0 3

ngas

3

-1 0 0 -0.2

-3 0 0 -15.0

-4 0 0 -0.2

#

Example 2:

boun

model 1

ti

2 0. 1.

pa

0.105 0.120

huf

0.01 0.001

ph

0.1 0.1

th

20. 20.

model 2

ti

2 0. 1.e20

pa

0.1 0.1

Model 1 has a constant air pressure source(pa). If the flow is in flow, the composition is determined by the flowing humidity (huf) conditions. This is applied to zone 1. Model 2 has a constant air pressure source and a flowing temperature. It is applied to zone 3

```
ft
20 20

-1 0 0 1
-3 0 0 2
-4 0 0 3
```

Example 3:

```
boun
model 1
ti
2 0. 1.
ph
0.1 0.1
th
20. 20.
hu
0.4 0.45
model 2
ti
2 0. 1.e20
pa
0.1 0.1
ft
20 20

-1 0 0 1
-3 0 0 2
-4 0 0 3

#
```

This example sets a fixed humidity 'hu'. In the algorithm, both water and air are added or removed as needed to main the fixed humidity condition.

Appendix C Description of source code changes (072616)